Numerical investigation of freak wave slamming on a fixed deck structure

Xin Wang[a], Min Luo[b,*], Harshinie Karunarathna[a], Jose Horrillo-Caraballo[a], Dominic E. Reeve[a]

[a] Energy and Environment Research Group, Faculty of Science and Engineering, Swansea University, Swansea SA1 8EN, United Kingdom

[b] Ocean College, Zhejiang University, Zhoushan 316021, Zhejiang, China

Abstract

Wave impact loads on box-shaped structures highly depend on the wave morphology. This paper conducts a numerical study of freak wave impacts on a fixed, box-shaped deck. A numerical wave flume characterized by enhanced momentum conservation is developed, showing satisfactory accuracy and stability in reproducing freak wave impacts. By changing the horizontal locations of the deck, comparative analyses of the kinematics and dynamics on the front, top and bottom walls of the deck are performed. Based on the morphological features of the wavefront and overturning wave tongue, a quantitative approach for classifying the impact types is proposed. Four impact types are identified, including the unaerated impact of a non-breaking wave, the well-developed plunging breaker impacts with air entrapment on the top or front wall, and the broken wave impact. By investigating the characteristics of each impact type, it is found that the wave shapes and impact behaviours vary significantly on the front and top walls but show high similarities on the bottom wall. The well-developed plunging breaker applies the largest wave pressures and forces, especially when air entrapment happens. Significant negative pressures appear on the top and bottom walls, and the sharp right angles on the edges of the front wall play an important role in the generation of such negative pressures. The influences of entrapped air pockets on wave loads highly depend on their locations. In particular, the entrapped air results in large pressures and insignificant air cushioning effects on the front wall. The findings of the present study would advance the knowledge of the breaking wave impact on box-shaped deck structures, especially the behaviours of the air entrapment and the influence on impact loads, which could underpin the design and assessment of coastal and ocean structures with deck platforms.

Keywords: Breaking wave; Ocean platform; REEF3D; Wave impact; Wave-structure interaction

[*] Corresponding author.
E-mail: min.luo@zju.edu.cn (M. Luo).

1. Introduction

Freak waves, also termed monster waves or rogue waves, pose substantial threats to ocean and coastal structures (Bitner-Gregersen and Gramstad, 2016; Hopkin, 2004). Freak waves are characterized by unusually large wave heights and power, which are more likely to create larger impact loads through a variety of hydrodynamic mechanisms (Qin et al., 2017). Hence, it is of practical importance to understand the fundamental mechanisms of freak wave impacts on coastal structures. A box-shaped deck is used in many coastal structures, such as oil/gas platforms, bridges and wharves. Such coastal structures are designed to withstand the 'front-on' impact of the waves, however, their failures due to extreme waves happen occasionally (Almashan et al., 2021; Attili et al., 2023a). This motivates the comprehensive study of the flow features, impact behaviours and wave load characteristics of the impact of freak waves.

Box-shaped structures can be idealised as rectangular decks with vertical walls front and rear and horizontal top and bottom walls. The horizontal lengths of decks are typically several times the thicknesses, which can lead to complicated flow fields and wave load distributions. Baarholm and Faltinsen (2004) studied the vertical loads of a regular wave train on the bottom wall of a box-shaped structure, and compared the predictions of boundary element and Wagner-based methods. Yan et al. (2019) studied freak wave impacts on a box-shaped structure and found the largest wave load when the impact took place before the wave breaking, while the wave impacts upon breaking and after breaking led to wave loads with similar magnitudes. Qin et al. (2017) compared the impacts of freak waves and regular wave trains, and found the steep wave walls of freak waves led to more severe impact loads and longer interaction durations. Filip et al. (2020) performed 500 numerical simulations of wave impacts on a fixed box-shaped platform and derived extreme-value probability distribution functions for the wave loads, and used these to characterise the dependence of wave load on wave steepness. Studies have also shown that the incident wave kinematics led to different amounts of overtopped water and varying wave loads on the top wall (Hu et al., 2017; Luo et al., 2020; Luo et al., 2022). Currently, various impact behaviours and effects have been observed, and no consensus has been obtained in terms of the impact behaviours and loads (e.g., the locations and values of the pressure maxima, and the corresponding impact scenarios).

Regarding the complicated impact behaviours, it is noticed in some studies that the wave impacts can be classified into different impact categories, by summarizing their similarities and characteristics. For example, Liu et al. (2019) studied the wave impacts on a vertical wall and categorized four types based on the distance between the breaking point and the wall and compared their behaviours. Zhou et al. (2024) classified four impact modes on the bottom side of a fixed plate based on aeration level and observed significant variations in pressure distributions among different modes. Zhang et al. (2024) identified four breaker types of wave impact on a square column with an overhanging deck, which took the speed of the breaker to establish the criterion. However, current classification standards tend to rely on qualitative measures, demonstrating a need for quantitative wave impact type identification, with the consideration of the morphology of the waves and the structures. More importantly, it is of great significance to find the most dangerous impact type on a box structure and to identify which part of the structure suffers more from the wave impact.

The entrapment of air may play a key role during the wave impact. The influence of entrapped air varies among different incident wave morphologies and entrapment locations. Studies have observed entrapped air pockets on the wave-facing walls, leading to the development of large pressures (Liu et al., 2019; Sun et al., 2019; Yan et al., 2019). In contrast, the air pockets entrapped on the top walls of the structures may result in low pressures or even negative pressures (Luo et al., 2022). Moreover, the entrapped air pocket may induce an air cushioning effect that reduces the impact pressure (Chuang et al., 2017). However, some other studies have not reported any such cushioning effect (Seiffert et al., 2015), and in certain cases, the entrapped air may even amplify the impact pressures (Bullock et al., 2007; Zhou et al., 2024). The problem becomes more complex when scaling the aerated wave impact to the prototype scale (Majlesi et al., 2024). As highlighted by Bullock and Bredmose (2024), it is crucial to understand the role of air entrapment during wave impacts for scaling. At different scales, the physical properties of the air pockets may vary significantly, such as the shape and size of the air pockets (Attili et al., 2023b), as well as the stiffness of the entrapped air (Bredmose et al. 2015). Compared with the frequently used Froude scaling law, the Bagnold-Mitsuyasu law (Bagnold, 1939; Mitsuyasu, 1966) has been recommended by Bullock and Bredmose (2024), and the authors have stated that a more rational and physics-based scaling law is still needed. These research questions and complexities necessitate further exploration of the development of air pockets and the surrounding flow fields.

To sum up, wave impacts on box-shaped structures involve complex physical processes in terms of morphology, kinematics and dynamics and no consensus has been reached yet. Numerical simulation has become an important tool in analysing complex wave-structure interaction problems (Chen et al., 2018; Mu et al., 2024). However, the accurate simulation of freak wave impacts, or more broadly breaking wave impacts, remains challenging due to the issues in handling the sharp change of fluid properties across the water-air interface (Pang et al., 2024; Raessi and Pitsch, 2012) and the non-conservation of mass and momentum associated with the highly-deformed interface (Cui et al., 2022; Liu et al., 2019; Shao et al., 2024). More specifically, the following aspects related to freak wave impacts need further investigation:

- Accurate simulation of the freak wave impact process and flow details;
- Identification of different freak wave impact scenarios and their characteristics;
- Exploration of the multiphase phenomena, such as air entrapment.

To address these points, we develop a numerical wave flume by employing the recently proposed Finite Difference Method (FDM) two-phase flow model with an enhanced momentum-conservation

(Wang et al., 2023). After validation against experimental results of freak wave impacts, we conduct simulations of the impact of a designed freak wave on a box-shaped structure with different horizontal locations. The kinematic and dynamic features under typical impact patterns are investigated. The investigation encompassed morphological characteristics of the waves, pressure distributions and wave forces on structure walls, as well as the air entrapments. The aims and objectives of this paper include:

- To illustrate the applicability and performance of the enhanced momentum-conservation treatment (Wang et al., 2023) in simulating the freak wave impact;
- To develop a quantitative identification of impact types, and study the kinematics and dynamics on each structure wall for different impact scenarios;
- To understand the morphological characteristics and role of air entrapment during freak wave impact.

The research contributions of the present study are three-fold. Firstly, the numerical wave flume advances the numerical tool for simulating freak wave-structure interaction. Secondly, a quantitative criterion is proposed for classifying the freak wave impact types. Thirdly, the kinematic and dynamic characteristics of the freak wave impacts on a deck structure, especially the role of air entrapment, are thoroughly investigated, which provides further insights into the physical process. In what follows, Sections 2 and 3 introduce the key formulations of the numerical method and the setup of the numerical wave flume, respectively. Section 4 presents a comprehensive validation of the developed numerical wave flume against experimental data. Using the validated numerical wave flume, 11 cases with different relative locations between the deck structure and the same incident wave are simulated and the results are presented in Section 5. After that, comprehensive discussions of the results are elaborated in Section 6, focusing on the morphological, kinematic and dynamic characteristics of freak wave impacts on the deck structure, and the air entrapment behaviours in different wave impact types. Finally, the research conclusions and findings are highlighted in Section 7.

2. Numerical methods

2.1. Governing equations

The numerical simulations in the present study are conducted using the code described by Wang et al. (2023). This is a modified version of the FDM-based CFD code REEF3D (version 20.02) (Aggarwal et al., 2020; Ahmad et al., 2020; Moideen et al., 2020). The governing equations are the incompressible Reynolds-Averaged Navier-Stokes (RANS) equations:

$$\frac{\partial u_i}{\partial x_i} = 0 \tag{1}$$

$$\frac{\partial u_i}{\partial t} + u_j \frac{\partial u_i}{\partial x_j} = -\frac{1}{\rho}\frac{\partial p}{\partial x_i} + \nu \left[\frac{\partial}{\partial x_j}\left(\frac{\partial u_i}{\partial x_j} + \frac{\partial u_j}{\partial x_i}\right)\right] + \frac{1}{\rho}\frac{\partial \tau_{ij}}{\partial x_j} + g_i \tag{2}$$

where u_i is the velocity, ρ the density, p the pressure, ν the kinematic viscosity, g_i the gravitational acceleration, and τ_{ij} represents the Reynolds stresses. The $k - \varepsilon$ model (Launder and Spaulding, 1974) has been adopted in the present study as the turbulence closure. The equations are as follows:

$$\frac{\partial(\rho k)}{\partial t} + \frac{\partial(\rho k u_i)}{\partial x_i} = \frac{\partial}{\partial x_i}\left[\frac{\mu_t}{\sigma_\varepsilon}\frac{\partial k}{\partial x_j}\right] + 2\mu_t S_{ij} S_{ij} - \rho\varepsilon \tag{3}$$

$$\frac{\partial(\rho \varepsilon)}{\partial t} + \frac{\partial(\rho \varepsilon u_i)}{\partial x_i} = \frac{\partial}{\partial x_i}\left[\frac{\mu_t}{\sigma_\varepsilon}\frac{\partial \varepsilon}{\partial x_j}\right] + C_1 \frac{\varepsilon}{k} 2\mu_t S_{ij} S_{ij} - C_2 \rho \frac{\varepsilon^2}{k} \tag{4}$$

where $S_{ij} = \frac{1}{2}(\frac{\partial u_i}{\partial x_j} + \frac{\partial u_j}{\partial x_i})$ is the strain rate tensor, and the eddy viscosity is computed as:

$$\mu_t = \rho C_\mu \frac{k^2}{\varepsilon} \tag{5}$$

Following Launder and Spalding (1974), the empirical coefficients C_1, C_2, C_μ, σ_k and σ_ε are taken to be 1.44, 1.92, 0.09, 1.0 and 1.3, respectively. The reasons for adopting the $k - \varepsilon$ model are twofold. First, in the simulation of breaking wave impacts, good accuracy is needed in predicting the morphological evolutions of the overturning plunging wave tongues (free shear flow) and the flow fields after the wave impacts (fully developed turbulence), and the $k - \varepsilon$ model is a suitable choice for modelling the abovementioned features (Bardina et al., 1997; Menter, 1994). Second, the $k - \varepsilon$ model provides satisfactorily good robustness (Attili et al., 2023a; Liu et al., 2024) and has been widely adopted to simulate breaking wave impacts on structures of various shapes (e.g., Attili et al., 2023a; Attili et al., 2023b; Hsiao and Lin, 2010; Jones et al., 2013; Pringle et al., 2016; Reeve et al., 2008; Wei et al., 2022).

2.2. Water-air interface capturing

The Level – Set method (Osher and Sethian, 1988) is adopted to capture the water-air interface. In the method, a Level – Set function φ is defined as the distance from a location to the water-air interface and its value is updated by solving an advection equation as follows:

$$\frac{\partial \varphi}{\partial t} + u_j \frac{\partial \varphi}{\partial x_j} = 0 \tag{6}$$

Re-initialization of φ is performed after the advection to maintain the signed distance property. According to the φ value, a Heaviside function is then defined as follows:

$$H(\varphi) = \begin{cases} 0, & if\ \varphi < -\zeta\Delta x \\ \frac{1}{2}\left[1 + \frac{\varphi}{\zeta\Delta x} + \frac{1}{\pi}\sin\left(\frac{\pi\varphi}{\zeta\Delta x}\right)\right], & if\ |\varphi| \le \zeta\Delta x \\ 1, & if\ \varphi > \zeta\Delta x \end{cases} \tag{7}$$

where Δx is local grid size, and ζ is a coefficient controlling the thickness of the interface region on which the Heaviside function is evaluated. For meshes close to the water-air interface, the fluid densities and viscosities are then computed based on the Heaviside function $H(\varphi)$, as follows:

$$\begin{cases} \rho_i = \rho_1 H(\varphi_i) + \rho_2(1 - H(\varphi_i)) \\ \nu_i = \nu_1 H(\varphi_i) + \nu_2(1 - H(\varphi_i)) \end{cases} \quad (8)$$

This numerical treatment suggests that the water-air interface is represented by an interfacial region of finite width $\zeta\Delta x$ towards both sides of the interface. Note that a thick interface provides smooth variations of fluid densities and viscosities across the interface and is advantageous for numerical stability (Khedkar et al., 2025), while a narrow interface models the physically sharp water-air interface better. Hence, the mesh size and ζ should be selected carefully for balancing accuracy and numerical stability. In the present study, the small-scale water droplets and air bubbles associated with the splashes after wave breaking are treated as water-air mixtures. Smoothing and averaging are used in the water-air interface region to give density and viscosity values for the water-air mixture. This handling approach may not precisely capture the real physics of small-scale water droplets and air bubbles and is a limitation of the present study.

2.3. Discretization schemes and numerical treatments

The governing equations are solved following the two-step projection method (Chorin, 1968). The ghost cell-based immersed boundary method (Berthelsen and Faltinsen, 2008) is used to model the solid wall boundaries. The 5th-order WENO scheme, i.e., WENO5 (Jiang and Shu, 1996), is used to construct the flux for the advection term. The 3rd-order Runge-Kutta TVD scheme, i.e., RK3-TVD (Gottlieb and Shu, 1998) is used for the time step propagation. The central difference and implicit Backward Time Centred Space (BTCS) schemes are used for the spatial and temporal discretization of the viscous term. An Enhanced Momentum Conservation (EMC) treatment has been implemented into the FDM model, which involves the momentum-based velocity reconstruction scheme, a strong temporal coupling between flow field solving and interface capturing, as well as measures to restrict the truncation errors during numerical discretization and the spatial mismatch between variables assigned on grid line centres and grid centres. More details of the numerical model are referred to Bihs et al. (2016) and Wang et al. (2023).

3. Setup of the numerical wave flume

A 2D numerical wave flume, as sketched in Fig. 1, is established to reproduce the 2D experimental case of Yan et al. (2019), where measurements were taken to ensure unidirectional wave impact on a well-positioned deck structure. A piston-type numerical wave maker is located at x = 0 m (see the coordinate system defined in Fig. 1). In numerical simulations of the experimental case, the piston motion time series measured in the experiment (which can be downloaded from the supplementary material) is used as the numerical input. The downstream end of the numerical flume is a wave absorption zone which employs the relaxation method (see e.g., Miquel et al., 2018) to dissipate wave energy and minimize wave reflections. An open boundary condition and a non-slip boundary condition are applied on the top border and the other borders of the computational domain, respectively. Variable time step sizes with the CFL number of 0.1 are adopted, and the interfacial thickness parameter ζ for the LSM is set to be 2.1, as suggested by Bihs et al. (2016). The turbulence model is only activated from the time instant when the wave touches the front-bottom corner of the deck for the cases not involving breaking waves or the time instant when the wave begins to break for the cases involving breaking waves.

Wave elevations are measured at three locations: x = 6.894 m (WG1); x = 9.659 m (WG2); and x = 11.104 m (WG3). Fluid velocities are measured by two velocity probes at 0.2 m beneath the still water level (SWL) with x = 6.847 m (VP1) and x = 11.269 m (VP2), respectively. A metallic box-shaped deck is deployed at 0.748 m above the flume bottom and the wave-facing side (which is called 'front wall' from here) of the deck is located at x = 12.557 m from the initial position of the wavemaker. The deck is fixed and hollow, with a length of 0.5 m (a) and a thickness of 0.12 m (b). Pressures at six locations on the deck are measured: two on the front wall with 0.035 m (FP1) and 0.08 m (FP2) to the bottom edge; two on the deck bottom (which is called 'bottom wall' from here) with 0.035 m (BP1) and 0.205 m (BP2) to the front wall; two on the deck top (which is called 'top wall' from here) with 0.038 m (TP1) and 0.083 m (TP2) to the front wall. A high-speed camera is located at the side of the flume, to capture the evolution of the wave during the impact.

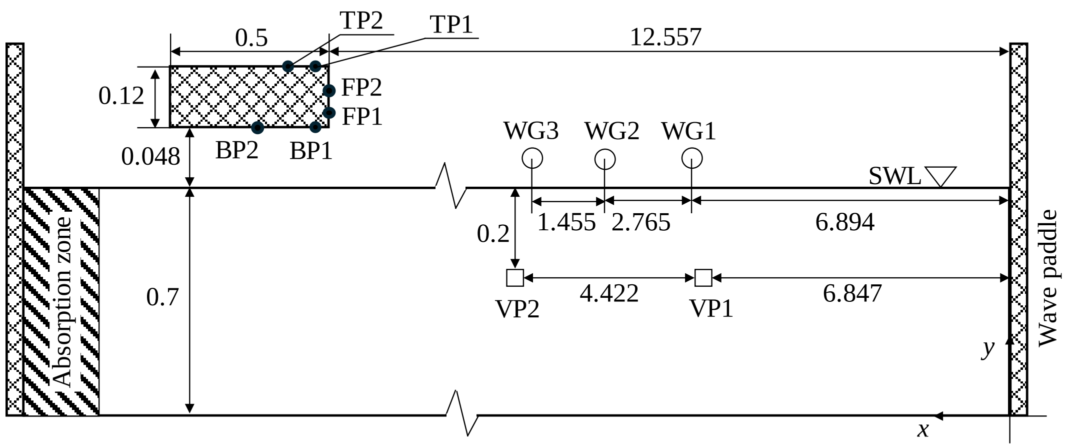

Fig. 1. Schematic view of the numerical wave flume (Unit: m).

Experimental data (Yan et al., 2019) are adopted to validate the numerical wave flume. In the experiment, freak waves were generated by using the wave focusing theory. Table 1 presents the parameters of the freak wave, in which h denotes the water depth, x_f the focusing distance from $x = 0$, x_d the location of the front wall. c_0 denotes the characteristic celerity of the freak wave. P_0 is calculated as $P_0 = \rho_{water} \cdot c_0^2$, which is the reference value for the normalization of the wave pressures (Blackmore and Hewson, 1984). P_N denotes the normalized pressure. For the normalization of the impact force, we adopted the wave slamming coefficient C_s (Jose and Choi, 2017), which is based on the semi-empirical formula proposed by Goda et al. (1966). As shown in Eq. (9), F_N is the normalized wave force, and A is the projected area of the structure normal to the wave propagation direction (in the present 2D study, $A = b \times 1$).

$$F_N = C_s = \frac{F}{F_0} = \frac{F}{0.5\rho_{water} \cdot A \cdot c_0^2} \tag{9}$$

Table 1. Parameters of the freak wave investigated in the present study.

Parameters	h (m)	x_f (m)	x_d (m)	c_0 (m/s)	P_0 (Pa)	F_0 (N/m)
Value	0.7	12.45	12.557	3.312	10948.5	656.8

The present numerical simulations replicate the laboratory setup of Yan et al. (2019), and based on the laboratory scale simulation results, the underlying physical mechanisms of the plunger-type freak wave impacts on a deck structure are studied. Hence, there is no scaling between numerical simulations and laboratory experiments. When scaling our results to real or prototype scales, the scaling needs to be carefully considered.

4. Mesh convergence test and validations

4.1. Mesh convergence test

A mesh convergence test is performed based on the four mesh resolutions shown in Table 2. The wave elevation histories over the time windows with the several large crests at the three wave gauges are presented in Fig. 2, and the pressure histories at the four pressure sensors (i.e., FP1, FP2, BP1 and BP2) are presented in Fig. 3. In general, the numerical results by the coarsest mesh, i.e. Mesh A, show significant discrepancies with other numerical results especially for wave impact pressures. With the refinement of mesh size, numerical results converge. Specifically, the time series of Meshes C and D almost overlap and are in closer agreement with the experimental data. The same trend is illustrated quantitatively by Table 3, which presents the relative errors of the wave elevation magnitudes (i.e., η_{max}) at the three wave gauges (i.e., WG1, WG2 and WG3) and the normalized pressure peaks ($P_{N\max}$) at four pressure measurement locations (i.e., FP1, FP2, BP1 and BP2). These results demonstrate the good accuracy of the developed numerical wave flume. In the following, Mesh D is adopted in simulations.

Table 2. Mesh settings in the mesh convergence study.

Mesh setting	Mesh A	Mesh B	Mesh C	Mesh D
Mesh size (m)	0.02 × 0.02	0.01 × 0.01	0.0075×0.0075	0.005×0.005

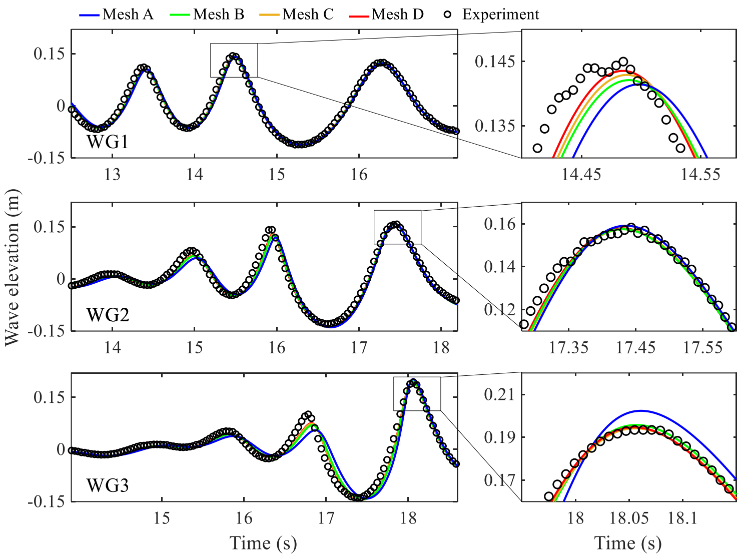

Fig. 2. Wave elevation histories produced by different mesh sizes.

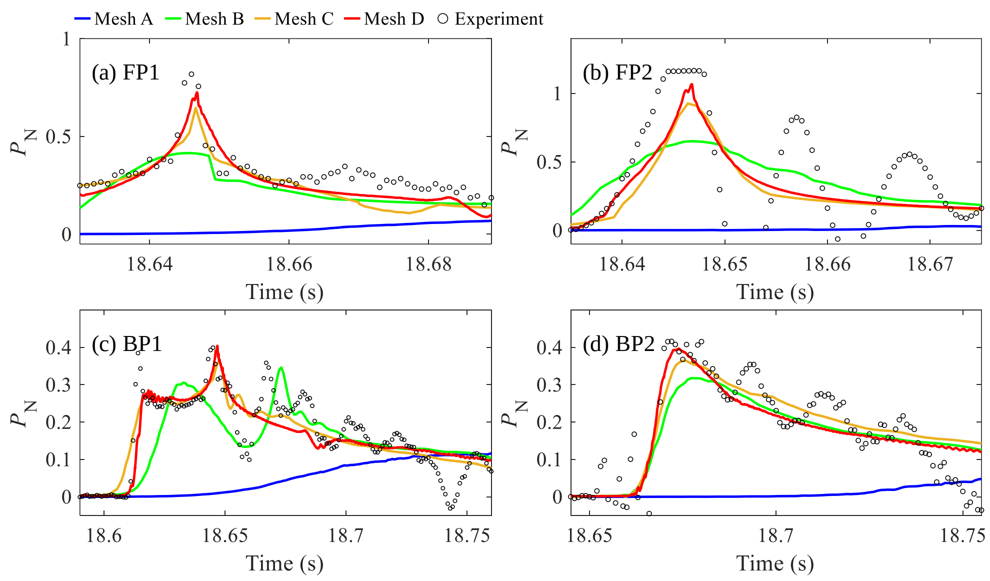

Fig. 3. Pressure time histories produced by the four mesh sizes at: FP1 (a), FP2 (b), BP1 (c) and BP2 (d).

Table 3. Relative errors of the maxima of wave elevations (η_{max}) and pressures (P_{Nmax}) for the four mesh sizes (absolute values of relative errors are presented).

Relative error (%)	Mesh A	Mesh B	Mesh C	Mesh D
η_{max} (WG1)	2.07	2	1.45	1.03
η_{max} (WG2)	0.1	1.01	0.94	0.75
η_{max} (WG3)	4.6	1.19	0.68	0.67
P_{Nmax} (FP1)	88.43	49.03	19.42	9.23
P_{Nmax} (BP1)	72.66	15.00	5.41	0.46
P_{Nmax} (FP2)	89.71	44.17	20.53	8.46
P_{Nmax} (BP2)	75.97	23.82	12.47	4.73

4.2. Validation against the experimental data

Fig. 4 presents the simulated flow velocities along the horizontal and vertical directions at VP1 and VP2. The developed numerical wave flume well simulates the velocity amplitudes and phases. Fig. 5 shows the wave impact pressures at the abovementioned six locations. In general, the present numerical wave flume successfully captures the magnitudes (both positive and negative) and evolution trends of the wave pressures on the front, bottom and top walls of the deck in the wave slamming process. Note that some discrepancies exist between numerical and experimental pressure histories. On the front wall of the deck, for example, the experimental data shows a high-frequency pressure fluctuation at FP2, while such fluctuations do not exist in the numerical results. Fig. 6 presents the experimental snapshots from 18.66 s to 18.68 s (time instants during the pressure oscillation period at FP2). It can be seen that FP2 is involved in the water-air mixing region (red curves in Fig. 6(a) to (c)). The propagating wave face applies forces onto this water-air mixture, leading to its compression and expansion and causing the pressure oscillations (Zhou et al., 2024; Ha et al. 2020). Since the present model adopts the incompressible fluid assumption and applies smoothing to the physical properties and water-air interactions at small scales, the pressure oscillations at FP2 are not reproduced. On the bottom wall, the experimental pressures at BP1 and BP2 oscillate synchronously, as shown in Fig. 7. This is related to the wave impact-induced structural vibrations that happen to the bottom wall of the deck, although stiffeners are installed inside this hollow structure. Since the present numerical model treats the deck structure as rigid, the pressure oscillations at BP1 and BP2 are not reproduced (see the middle column of Fig. 5).

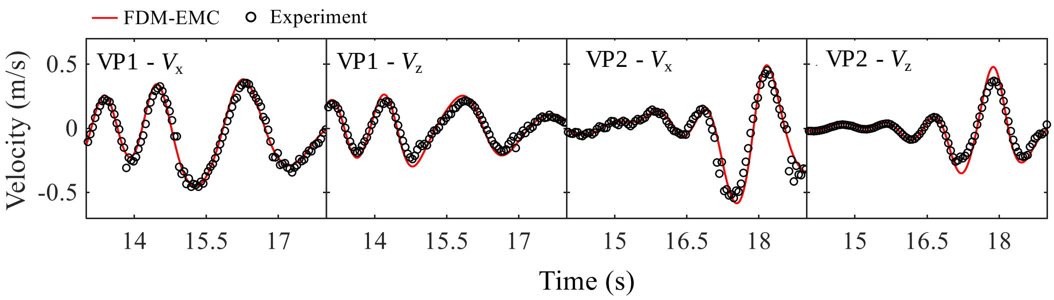

Fig. 4. Comparison of numerical and experimental results of the velocity components.

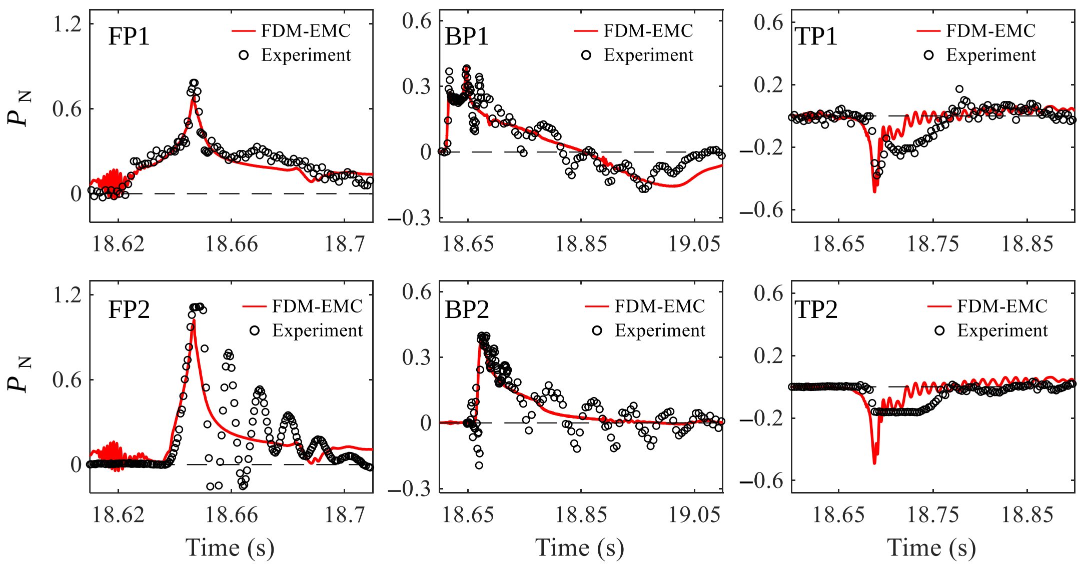

Fig. 5. Normalized pressures at the pressure sensors on the deck (black dashed line stands for zero pressure).

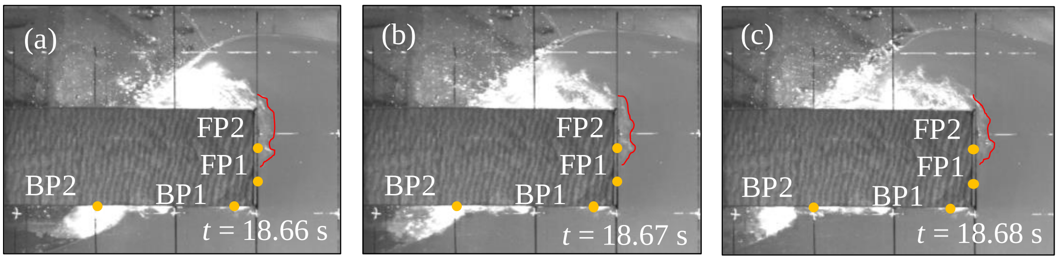

Fig. 6. Experimental snapshots of the wave impact at: (a)18.66 s, (b)18.67 s and (c)18.68 s. The red curves show the regions of water-air mixing on the front wall.

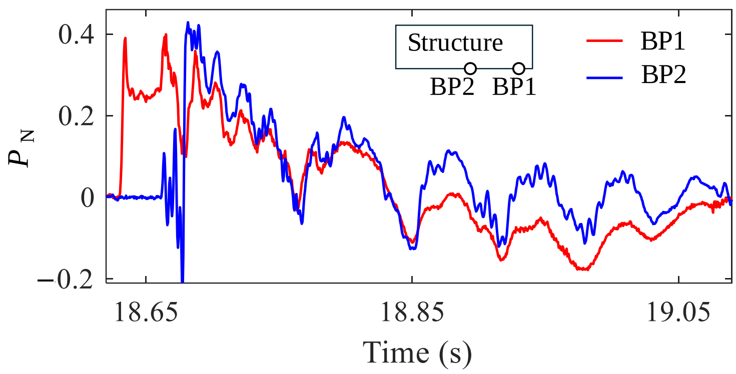

Fig. 7. Synchronous oscillation of experimental pressure histories at BP1 and BP2.

The simulated wave profiles are compared with the experimental snapshot at typical time instants, as shown in Fig. 8. It can be seen the simulated water-air interface agrees well with the experiment snapshot, even after the wave slamming on the front wall. It is noted the FDM-EMC scheme maintains a smooth shape for the water-air interface during the impact, indicating the good performance of the EMC treatment with respect to numerical stability and interfacial smoothness. In summary, the FDM-EMC scheme has shown a good level of numerical stability and accuracy, allowing the exploration of flow details of the highly deformed freak wave.

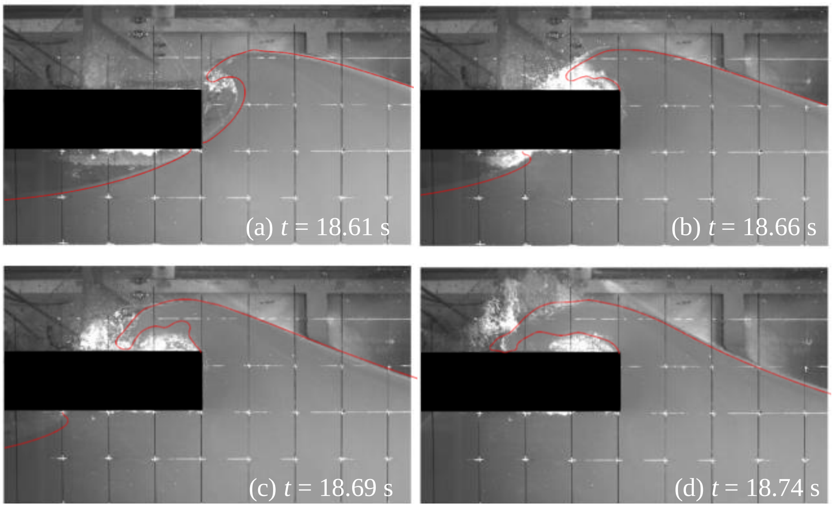

Fig. 8. Wave profiles reproduced by the developed FDM-EMC model (red solid curves) in comparison with experimental snapshots at: (a) 18.61 s, (b) 18.66 s, (c) 18.69 s and (d) 18.74 s.

5. Breaking wave slamming with varying horizontal locations

A deck structure may experience impacts by waves of different shapes. Previous studies have shown that the wave shape upon impact is a key factor in determining the dynamics (Huang et al., 2022; Zhang et al., 2024). To explore the breaking process and analyse the impact types and behaviours, we adjust the horizontal locations of the structure (x_d), to allow the designed freak wave to impact as an unbroken, breaking and broken wave. In this regard, ten more numerical cases are performed, as shown in Table 4. Together with the experimental case in the previous section (Case 0), the timelines of these 11 numerical cases are synchronized, based on the time instant when the front-bottom corner of the deck gets wet (t_0).

Table 4. Locations of the deck (x_d) and reference time (t_0) of each case.

Case #	Case 0	Case 1	Case 2	Case 3	Case 4	Case 5
x_d (m)	12.557	12.107	12.207	12.307	12.407	12.507
t_0 (s)	18.60	18.37	18.42	18.47	18.52	18.57
Case #	Case 6	Case 7	Case 8	Case 9	Case 10	
x_d (m)	12.607	12.707	12.807	12.907	13.007	
t_0 (s)	18.62	18.66	18.70	18.74	18.80	

5.1. Impact processes of different impact types

5.1.1. Conceptual classification of impact types

Throughout the entire impact process, the evolutions of the water-air interface of each case are presented in Fig. 9. It can be seen that for all numerical cases, the simulated water-air interfaces maintain smooth shapes during the entire impact process, demonstrating good numerical stability and interface smoothness of the FDM-EMC model. Fig. 10 shows the time histories of the six pressure transducers (FP1&2, BP1&2 and TP1&2). According to Figs. 9 and 10, the pressure histories and wave shapes, especially the evolutions of the wave tongues, display common features among different types. We take these 11 numerical cases, including different impact patterns, and categorize them into four types.

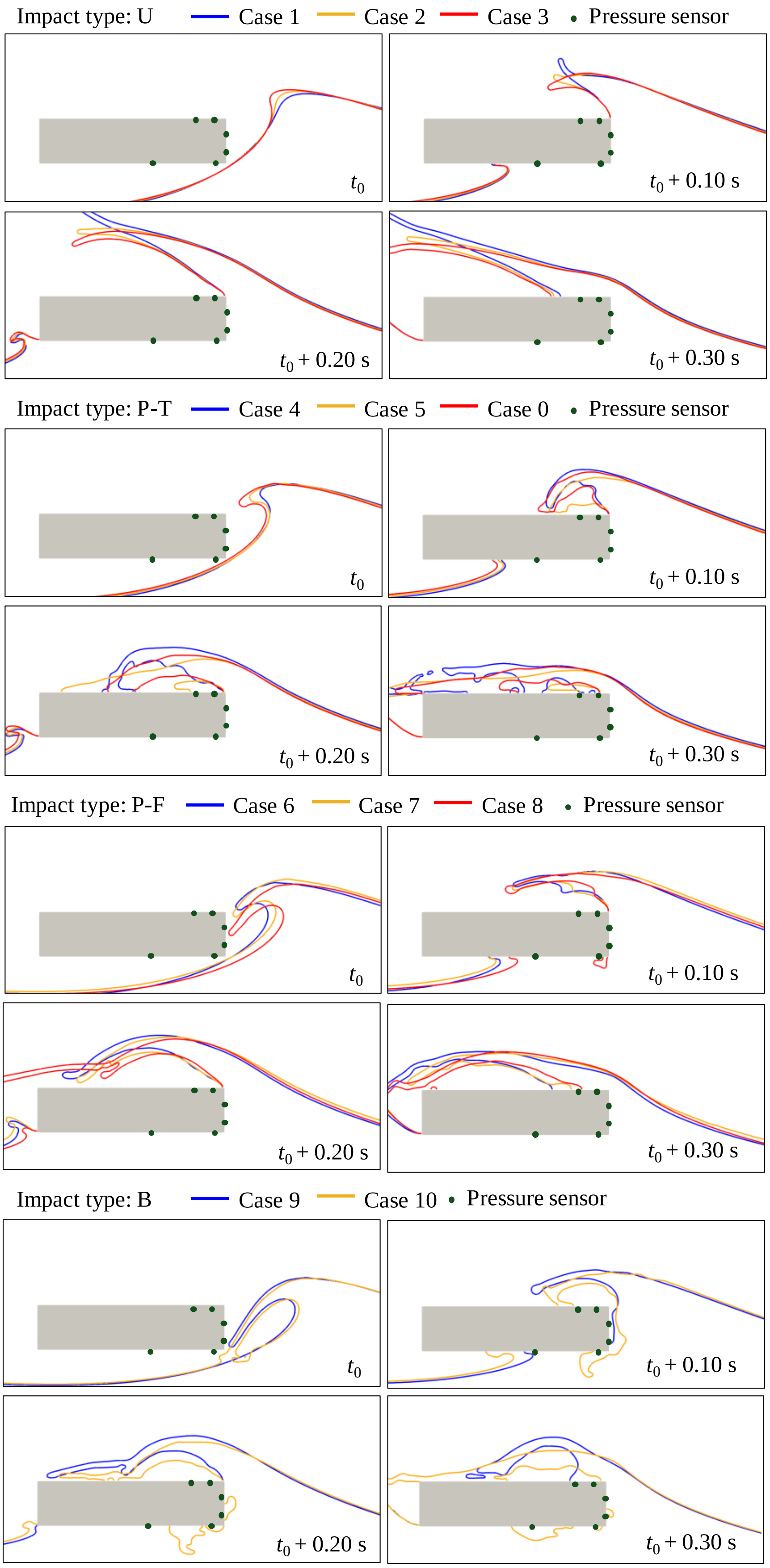

Fig. 9. Evolutions of wave profiles during wave impacts for all numerical cases.

Cases 1 to 3 are labelled as ‘Unbroken wave impact (U)’, as the wavefront is still developing upon the impact. No air entrapment is detected and all pressure transducers show single pressure peaks. Cases 4 to 8 and Case 0 feature a well-developed plunging wave shape at impact. Cases 4, 5 and 0 show air entrapment on the top wall, while the pressure transducers on the top wall (TP1&TP2) present significant negative pressure. Hence, Cases 4, 5 and 0 are labelled as ‘P-T’ (Plunging impact with Top wall air entrapment). For Cases 6 to 8, air entrapment is observed on the top wall, and the pressure transducers on the front wall (FP1&2) show a large initial peak followed by a lower peak. Thus, we label Cases 6 to 8 as ‘P-F’ (Plunging impact with Front wall air entrapment). Cases 9 and 10 are characterised by an over-developed broken wave shape at impact, and the overturning tongues directly hit the front wall, resulting in the double-peak pressure histories on the front wall. Therefore, Cases 9 and 10 are classified as ‘B’ type (Broken wave impact).

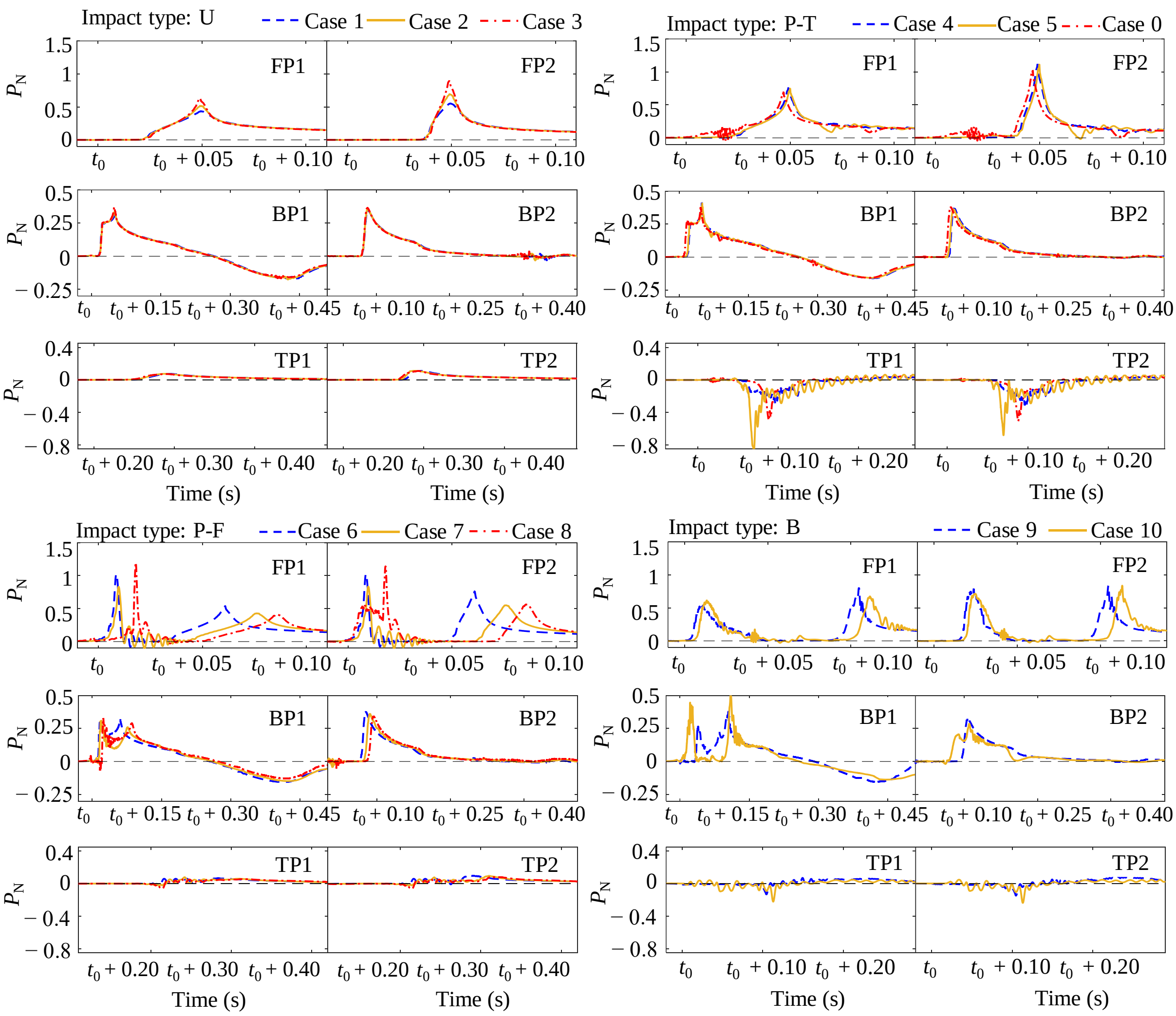

Fig. 10. Pressure histories at the six considered locations for all numerical cases.

According to the great similarities of the cases within the same impact type, we pick one representative case to illustrate each impact type with brevity, i.e., Cases 2, 5, 6 and 9 for U, P-T, P-F and B types, respectively. It is noted these classifications are qualitative for now, but a quantitative classification standard will be provided in Section 5.1.3.

5.1.2. Impact processes of different wave impact types

Unique features are observed for each impact type, especially for the early stage of the impact process. Fig. 11 presents the wave profiles, velocity vectors and pressure contours at typical time instants of the representative case in each impact type. Fig. 12 presents the pressure histories of FP1, BP1 and TP1, as well as the velocity histories in the vicinity of the pressure measurement locations (one grid away perpendicular to the structural walls). By comprehensively considering the wave profiles and pressures (Figs. 9 to 11), the time series in Fig. 12 can be divided into several stages based on the dominating features, i.e., air entrapment, wave tongue impact and wave face impact (the dot-dashed lines in Fig. 12 approximately separate the impact stages).

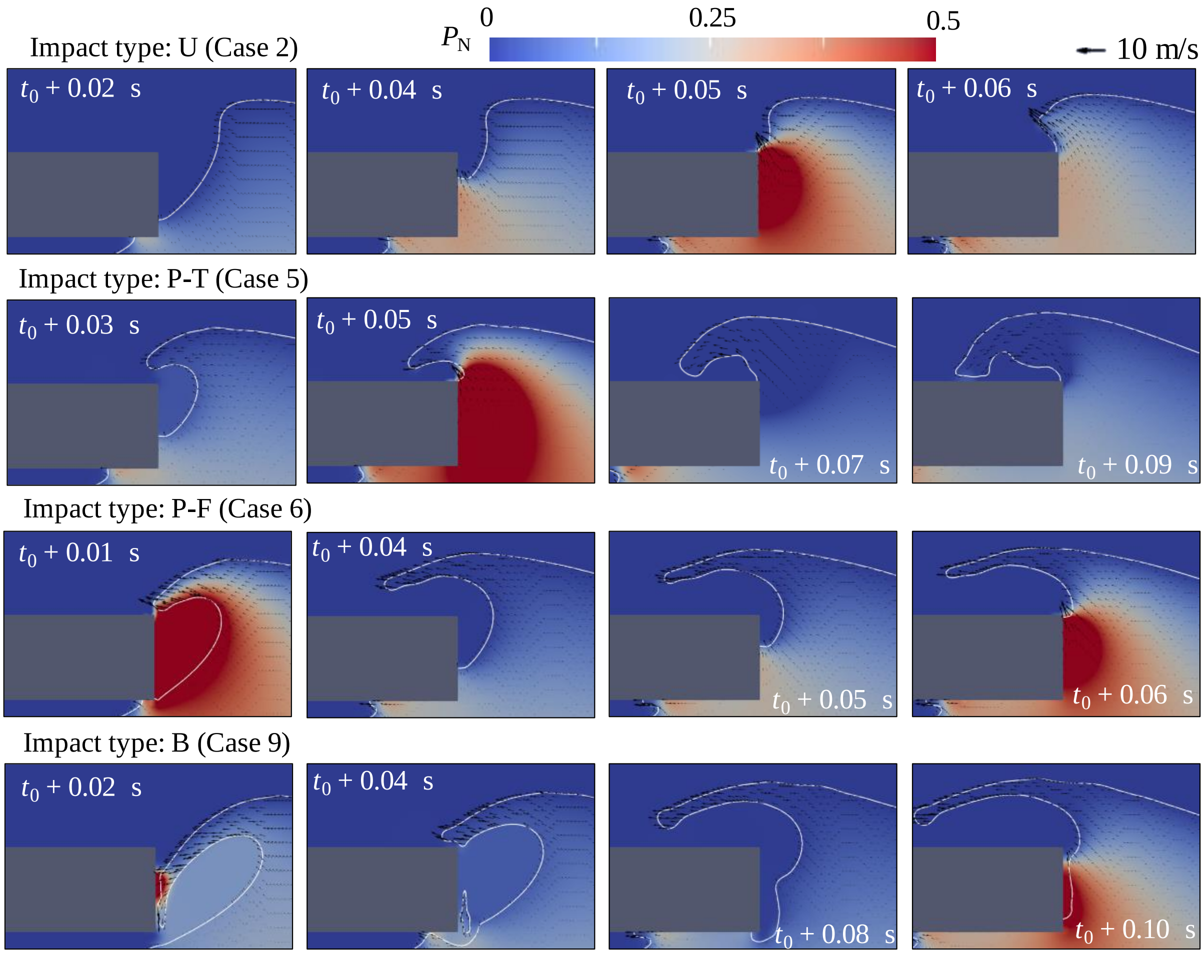

Fig. 11. Wave profiles, pressure contours and velocity vector fields at typical time instants of representative cases in the four impact types.

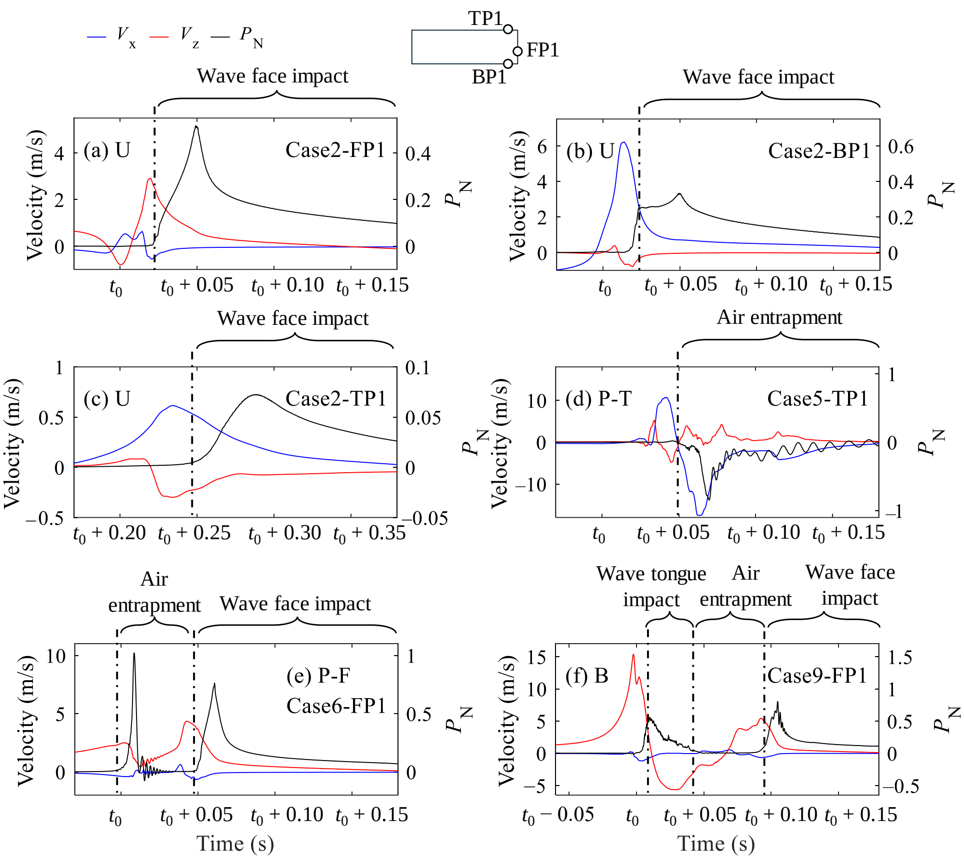

Fig. 12. Pressure histories at FP1, BP1 and TP1, as well as the velocity histories in the vicinity of the pressure measurement locations (one grid away normal to structural walls), for the four impact types.

The U type impact manifests the impact of unbroken waves, which coincide with the 'upward deflected breaker' and 'spilling breaker' identified by Zhang et al. (2024). It can be seen from Fig. 12 (a) to (c) that the airflow prior to the wave face impact leads to negligible pressures, and the water flows pass through the pressure measurement locations of FP1, BP1 and TP1 with decreasing velocities and increasing pressures. Note that the pressure peaks always happen shortly (~ 0.05 s) after the velocity peaks. On the front wall, the upward climbing wave face reaches the top-front edge of the deck prior to the advancing wave tongue, which is accompanied by a high-pressure area and an upward-shooting water jet with high velocity (first row of Fig. 11). This jet brings large upward velocity into the wave tongue, resulting in the most significant vertical stretch of the water tongue among the four wave impact types.

The P-T type features a plunging breaker and an enclosed air pocket on the top wall (the second row of Fig. 11). By the time the upward climbing wave face reaches the front-top corner, the advancing wave tongue has already moved beyond the front wall (but has not hit the front wall). The overturning tongue falls quickly on the top wall, with an enclosed air pocket captured (the snapshots at t_0 + 0.07 s in the second row of Fig. 11). According to Fig. 12(d), the captured air flows with a high velocity at the order of 10 m/s, associated with a large negative pressure at TP1 ($-0.84\rho c^2$). Such high-velocity airflow and large negative pressure only last for ~ 0.02 s. While the impact process on the top wall depends both on the water tongue and air, the impact process on the front wall of the P-T type is still dominated by the wave face, which shows high similarity with that of the U type (see the first and second rows of Fig. 11).

The P-F type also shows a violent plunging breaker like the P-T type. However, the overturning tongue hits the front wall while the wave face is still rising. Thus, the enclosed air pocket is captured on the front wall instead of the top wall (see the third row of Fig. 11). This air pocket is associated with the declaration of the airflow and a transient high pressure (~ 1.00 ρc^2) prior to the impact of the wave face, as can be ben seen from Fig. 12(e). The transient high pressure in the air pocket applies an upward force to the wave tongue, making the tongue slightly lifted (Fig. 9), which re-establishes the connectivity between the air pocket and atmosphere and enhances the air leakage with an increased velocity (see the air entrapment stage in Fig. 12(e)). After this, the impact of the wave face leads to a similar process on the front wall to the U and P-T types (see Fig. 11 and the wave face impact stage in Fig. 12(a) and (e)).

The B type represents the impact of broken waves with the most developed overturning tongue among the four types (see the fourth row of Fig. 11). The overturning tongue hits the front wall, leading to the declaration of the water flow and a pressure rise (see Fig. 12(f)). By analysing Figs. 11 and 12(f), it can be observed that the captured air pocket applies insignificant pressures on the front wall, and the captured air escapes with an increasing velocity due to the air leakage. The impact of the wave tongue generates a downward-shooting jet, which penetrates into the underlying wave face and brings intensive water-air mixing. The flow mixing between the downward jet and the propagating wave forms a nearly vertical wave face, which impacts on the front wall after the air leakage and results in a high-pressure area on the front wall.

The spatial distribution of fluid turbulence during the wave impact process is analysed through plotting the contours of the product of turbulence kinetic energy (TKE) and fluid density ρ (a quantity related to the Reynolds stress), and the velocity vector fields for each impact type, as shown in Fig. 13. For all impact types, turbulence in the water flows is mainly generated by the direct impacts of wave faces or wave tongues and the water-air mixing induced by the upward-shooting air jets. Flow separations occur at the front-bottom corner of the deck, and the water flows hitting on the front and bottom walls experience significant velocity reductions. The high velocity gradients in the local regions around the leading edges of the water flows lead to relatively large Reynolds stresses (e.g., the value TKE$\times\rho$ being around 200 Pa on the front wall and 100 Pa on the bottom wall), which transport with wave propagation (see the green circles in Fig. 13). The direct impact of the wave face entraps air on the front and bottom walls of the deck and squeezes the air regions. The air is accelerated from ~ 1 m/s to ~ 10 m/s and escapes upwards and leftwards along the deck walls. The upward-shooting jets then meet the horizontal-moving wave tongues, leading to significant changes in airflow directions, large gradients of local air velocities and intensive water-air mixing (see the red boxes in Fig. 13). As a result, relatively large areas with high Reynolds stresses (TKE×ρ reaching ~ 1000 Pa) are observed in the water flows above the top wall, subsequently after the direct impact of the wave face. Strong turbulence primarily appears at the leading tips or rear parts of the overturning tongues, depending on the morphologies of the overturning tongues of different wave impact types. Also note that the impact type B is more aerated upon the impact, due to the penetration of the wave tongue into the underlying wave face (see Section 5.1.1 and Fig. 13(d)). Water-air mixings occur at the front-bottom corner and the front wall, accompanying relatively large areas with turbulence and significant reductions in impact pressures. As shown in Fig. 10, the pressures reduce from ~ $0.5\rho c^2$ to less than $0.1\rho c^2$ at BP1 within 0.05 s in the B-type impact.

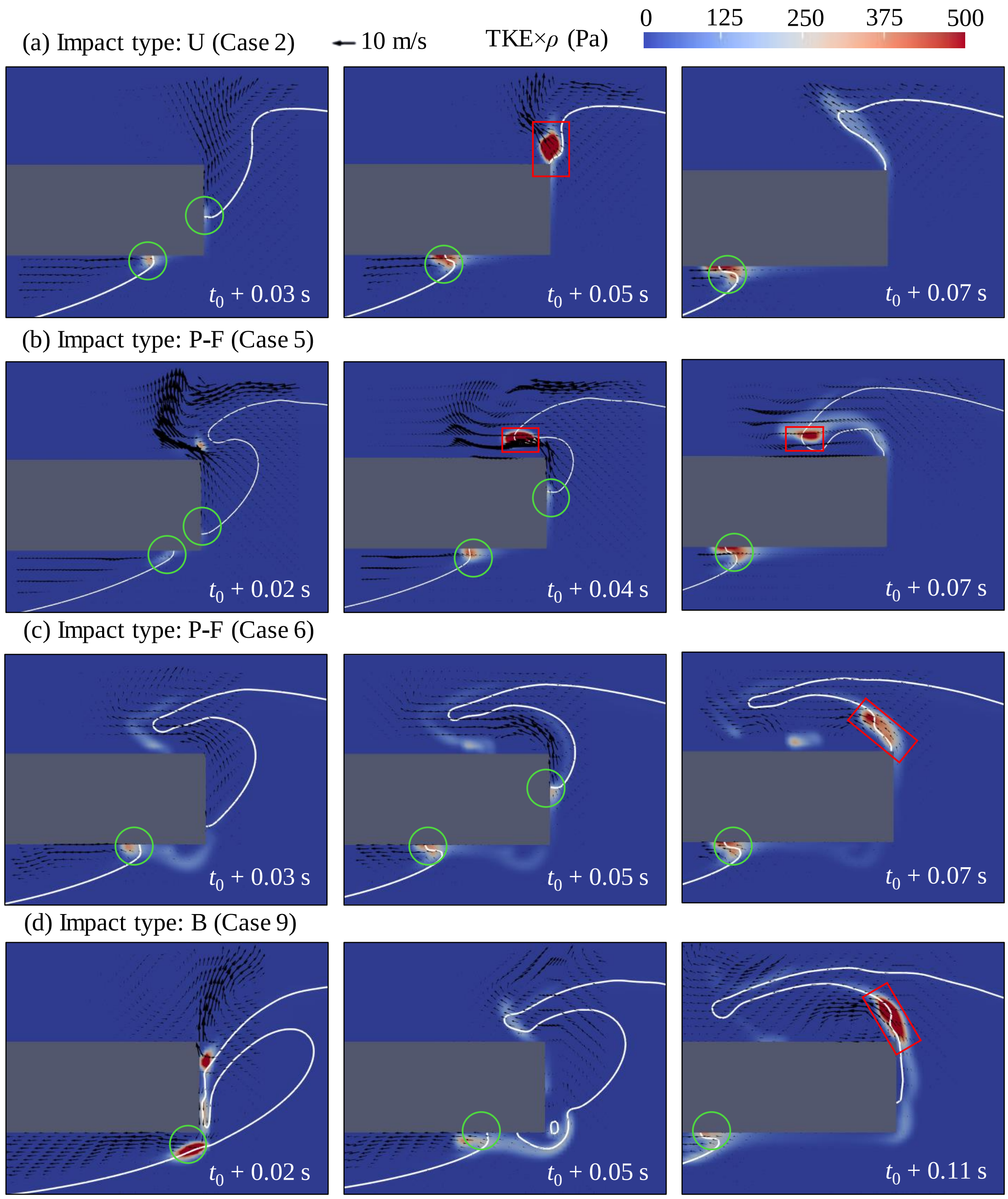

Fig. 13. Contours of TKE×ρ and velocity vector fields at typical time instants: (a) U type, (b) P-T type, (c) P-F type and (d) B type.

Fig. 14 presents the time histories of TKE×ρ and flow velocities in the vicinity of FP1 and BP1 (one grid away from the structural wall), which are also divided into different stages based on the dominating processes (air entrapment, wave tongue impact and wave face impact, water-air mixing). As can be seen, prior to the direct impacts of wave faces or wave tongues, the airflows at FP1 and BP1 are accelerated. Due to the relatively small values of TKE×ρ associated with these airflows (below 50 Pa), the airflow turbulence does not significantly influence the water flows upon the wave impact. For all impact types, at both FP1 and BP1, the Reynolds stresses reach the peak values around 0.01 s after the start of the wave face or wave tongue impact. The water flow velocities reduce quickly (within 0.05 s) and the Reynolds stresses dissipate rapidly. Note that the wave tongue impact in the B type (see the top right plot in Fig. 14) leads to the largest Reynolds stress at FP1 (TKE×ρ ≈ 200 Pa) among the four impact types, which also lasts longer than the Reynolds stress at FP1 induced by the subsequent wave face in the B-type impact.

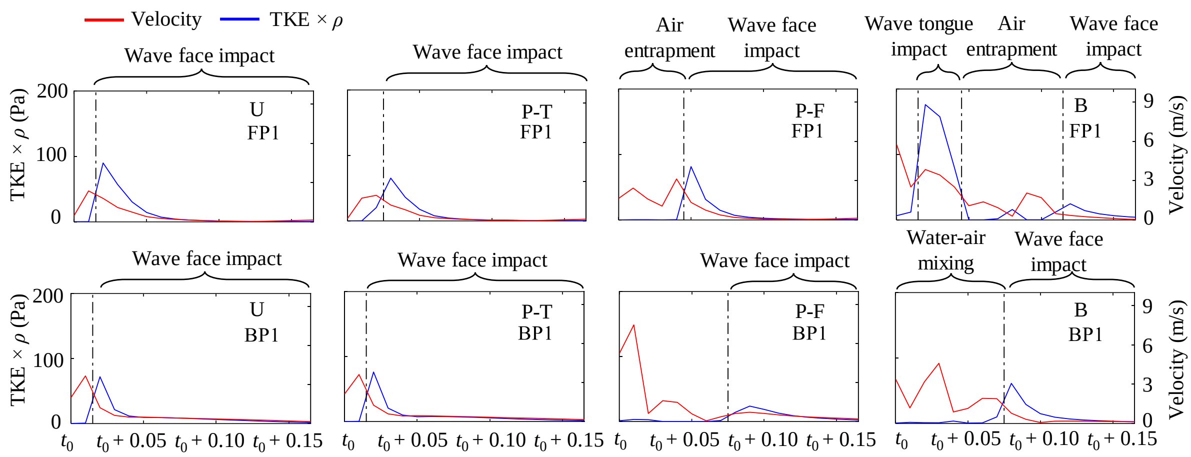

Fig. 14. Time histories of TKE×ρ and fluid velocities for the four impact types (top row: FP1; bottom row: BP1).

5.1.3. Quantitative classification for impact types

Fig. 15 presents a typical wave profile for illustration. The top part with the overturning water jet is termed the ‘wave tongue’, whose leading edge is the ‘wave tip’; the inclined front of the incoming wave bulk is the ‘wave face’. Morphological parameters have been used by relevant studies to quantitatively classify the impact types (Zhang et al., 2024). In our study, we do not only consider the morphological parameters, but also the parameters describing the movements of the water tongue and advancing wave face, which control the evolution of the wavefront. Six parameters are introduced: the relative height between the top of the breaking tongue and the top wall (δ_1); the relative height between the wave tip and the top wall (δ_2); the horizontal distance between the wave tip and front wall (δ_3); the horizontal and vertical velocities of the tip of the wave tongue (U_{tx} and U_{ty} respectively); the vertical velocity of the upward-climbing wave face (U_{fy}). Taking t_0 as the reference time, we define two parameters: the duration for the wave tongue to reach the same horizontal position as the front wall (T_1), which can be calculated as $T_1 = \delta_3/U_{tx}$; the duration for the climbing wave face to reach the front-top corner (T_2), which can be calculated as $T_2 = b/U_{fy}$.

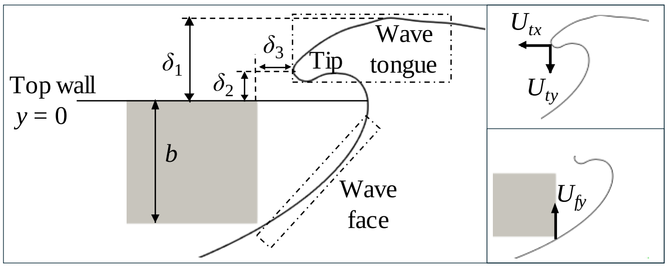

Fig. 15. Sketch of the wave slamming and the morphological parameters for the breaking wave, i.e. δ_1, δ_2, δ_3, U_{tx}, U_{ty} and U_{fy}.

As described earlier, for the U type, the wave face reaches the vicinity of the front-top corner prior to the wave tip, requiring $T_1 > T_2$. In contrast, the wave tip arrives in the vicinity of the front-top corner earlier than the wave face for P-T and P-F types, requiring $T_1 < T_2$. For the P-T type, the tongue is still vertically higher than the top wall at $t_0 + T_1$, thus $|U_{ty} \times T_1| < \delta_2$ and $\delta_2 > 0$. For the P-F type, to capture the air pocket on the front wall, the overturning tongue needs to be vertically lower than the top wall at $t_0 + T_1$, meanwhile, the tip of the tongue should not be lower than the bottom wall, thus, P-F requires $|U_{ty} \times T_1| > \delta_2$ and $\delta_2 > -b$. For the B type, the air pocket is captured between the tongue and the wave face before the impact, and the tongue tip has already descended to the wave face at t_0, thus $\delta_2 \leq -b$. These criteria can be used as guidelines for identifying wave impact types, as presented in Table 5.

Table 5. Classification of impact types (the underlines indicate the representative cases of different types).

Types	Case #	Features	Morphological properties at t_0
Unbroken wave impact (U)	1, 2, 3	No noticeable breaker; Upward-shooting tongue after the impact	$T_1 > T_2$
Plunging wave with top wall entrapment (P-T)	4, 5, 0	Plunging breaker impact on the front wall; Air entrapment and fast-falling tongue on top wall	$T_1 < T_2$ & $U_{ty} \times T_1 < \delta_2$ & $\delta_2 > 0$
Plunging with front wall entrapment (P-F)	6, 7, 8	Plunging breaker impact and air entrapment on the front wall; slightly lifted tongue after the impact	$T_1 < T_2$ & $U_{ty} \times T_1 > \delta_2$ & $\delta_2 > -b$
Broken wave impact (B)	9, 10	Broken wave impact and water-air mixing on the front wall	$\delta_2 \leq -b$

5.2. Impact pressures, forces and impulses

5.2.1. Wave profiles and resulting pressures

According to Section 5.1, the impact process consists of three main components: the impact of the wave face, the effect of the entrapped air and the impact of the wave tongue. To investigate their resulting pressures and their relationships with the wave morphology, we present the evolutions of pressures along the structure walls and the water-air interfaces in Figs. 16, 17 and 18 for the front, bottom and top walls, respectively.

The front wall of the deck is subjected to the wave face impact for all types, and the air entrapment (P-F) and the wave tongue impact (B) affect the front wall prior to the wave face impact. For the wave face impacts of U, P-T and P-F types (Fig. 16 (a) to (c)), evident similarities in the wave face shape and the resulting pressure evolutions are observed, which are characterized by the high pressure at the top of the wetted area. In comparison, the nearly vertical wave face in B type leads to a simultaneous pressure rise for the entire wetted area. The compressed air pocket in P-F results in evenly distributed pressures on the front wall, with the magnitude even higher than the wave face impact (Fig. 16 (c), t_0 + 0.01 s). B shows the impact of the overturning wave tongue, which only led to the pressure rise in a small area of contact (Fig. 16 (d), t_0 + 0.01 s). Linking with the histories of pressures (Fig. 10), it is seen the wave face leads to the unique pressure peaks of U and P-T, as well as the second pressure peaks for P-F and B on the front wall. The first pressure peaks for P-F and B result from the air entrapment and wave tongue, respectively.

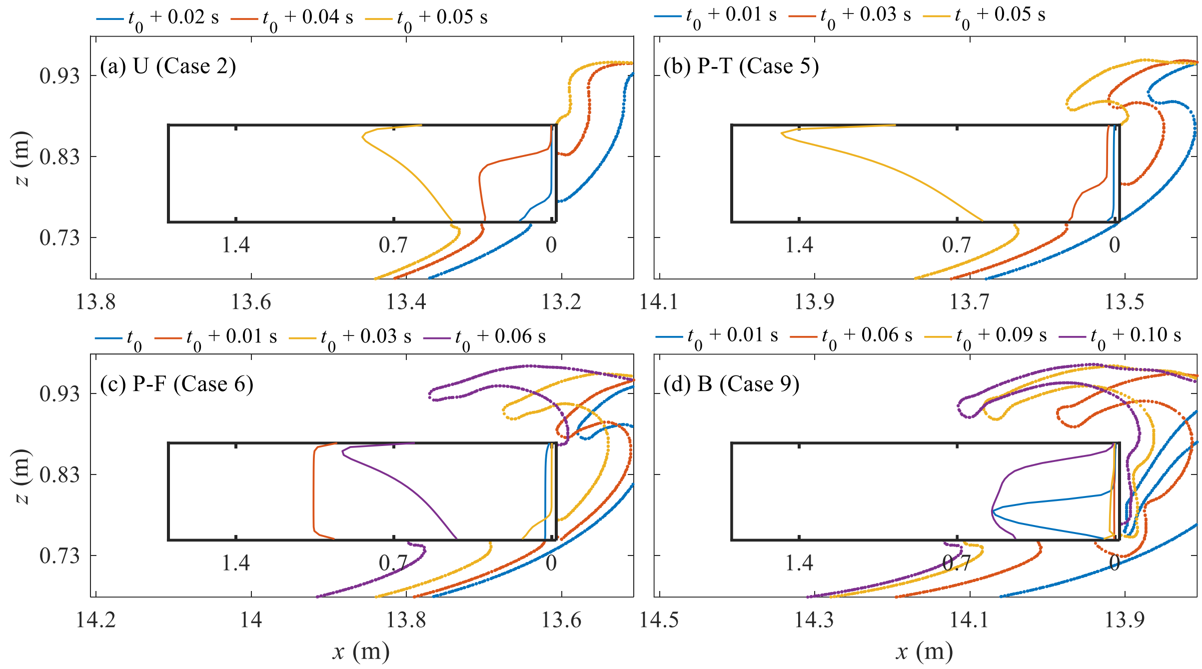

Fig. 16. Wave profiles and pressure along the front wall at typical time instants for the four types. The inner box resembles the box-shaped deck, and the *x*-axis of the inner box denotes the normalized pressure (P_N). (a) to (d) represent U, P-T, P-F and B types, respectively.

On the bottom wall, the wave face impact is the major contribution to the impact process, and the shapes of the wave faces are highly similar for all four impact types (see Fig. 9), leading to nearly identical pressure distributions (which will be shown in Section 5.2.2). Thus, we only present the results of the P-T type (Case 5). According to Fig. 17(a), the wave face passes along the bottom wall without significant change in shape. Similar to the wave face climbing on the front wall for the U, P-T, P-F types, the wave face on the bottom wall also generates a high pressure behind the advancing wave face. At the late stage of the wave impact (Fig. 17(b)), negative pressure appears with the falling wave profile to the upstream side of the front wall. This negative pressure has been termed the 'suction effect' by several authors (e.g. Sun et al., 2019; Wang et al., 2022; Duong et al., 2022; Wang et al., 2024). The centre of this negative pressure area moves downstream slightly, with the peak negative pressure dipping to ~ − $0.16\rho c^2$ before returning to zero.

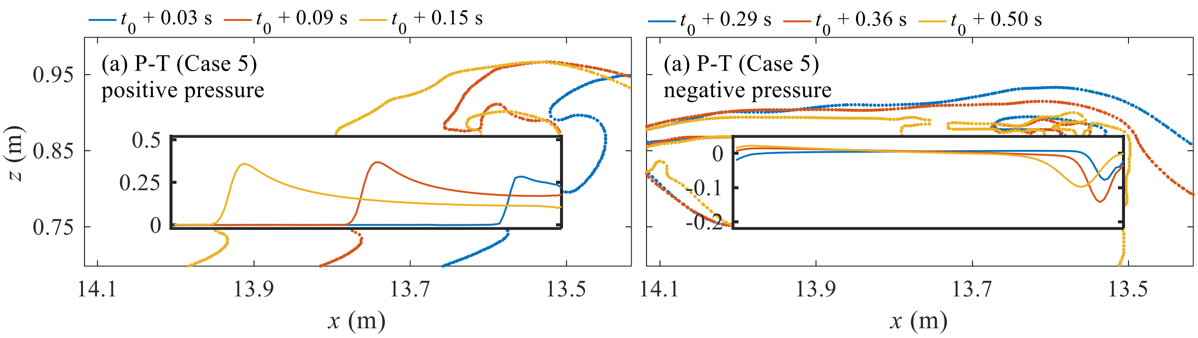

Fig. 17. Wave profiles and pressure distributions of P-T (Case 5) at typical time instants: (a) impact with positive pressures; (b) water receding with negative pressures. The inner box resembles the box-shaped deck, and the *y*-axis of the inner box denotes the normalized pressure (P_N).

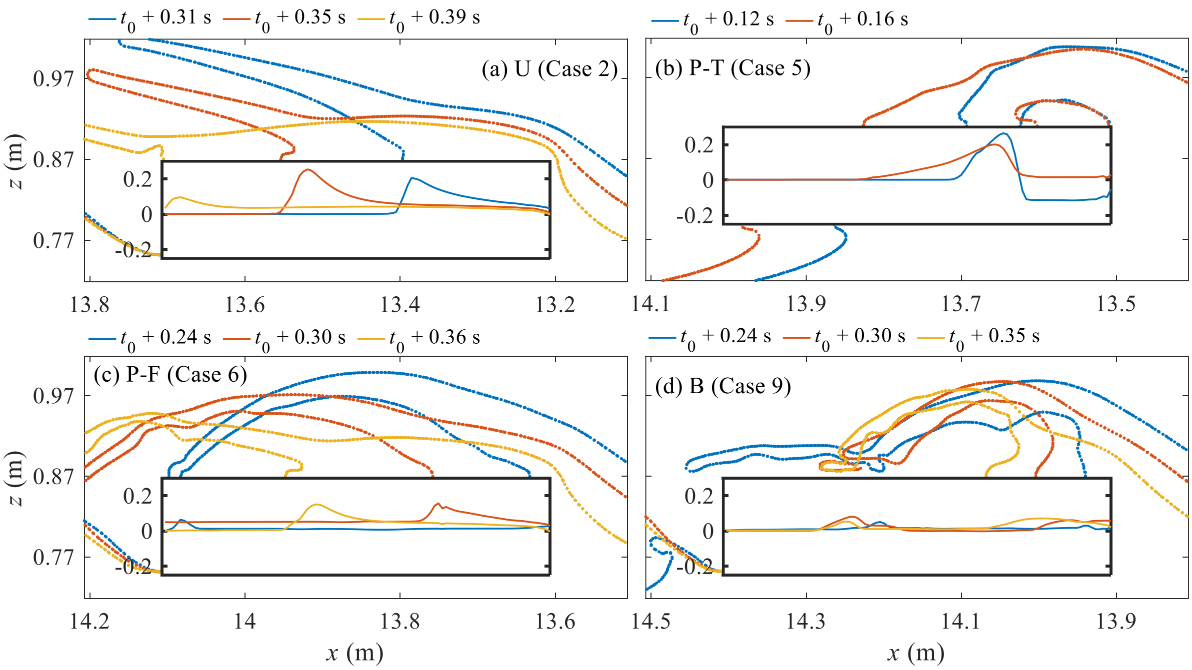

Fig. 18. Wave profiles and pressure distributions on the top wall for each impact type at typical time instants. The inner box resembles the box-shaped deck, and the *y*-axis of the inner box denotes the normalized pressure (P_N). (a) to (d) represent U, P-T, P-F and B types, respectively.

On the top wall, the major contributions to the impact involve wave tongue and air entrapment. According to Fig. 18, the wave tongue directly hits the top wall with its tip for all types except U type, creating a high pressure at the area of contact. In contrast, the wave tongue of U type slams on the top wall while the tip is still in the air, resulting in a larger high-pressure area moving forward. The rising wave face reaches the top wall in all four types but does not lead to a significant pressure rise. It is noticed in the P-T type (Fig. 18(b)), that the significant negative pressure is evenly distributed on the top wall in the vicinity of the front-top corner, which highly coincides with the captured air pocket on the top wall. Such a phenomenon has been rarely reported in the literature, which will be discussed in Section 6.3.2.

To sum up, the pressure induced by wave face impact highly depends on the shape of the incident wavefront, especially on the front wall. The similar wave shapes on the front and bottom walls result in similar pressure evolutions. The air entrapment on structure walls leads to evenly distributed high pressure, while the impact of the wave tongue tip results in the high pressure in a small area of contact. Two types of negative pressures are observed, one appears on the front-bottom corner at the late stage of the impact for all types ('downward suction effect'), and the other one appears above the front-top corner for the P-T type ('upward suction effect'). The influence of the wave profile and structure shape on the wave impact pressure will be discussed in Section 5.2.

5.2.2. Pressure distributions, force histories and impulses

To explore the relationship between the pressure and forces on the deck and illustrate the evolutions of wave loads comprehensively, we present the spatio-temporal pressure distributions on the structure walls, as shown in Fig. 19. By integrating the pressures on the walls, we obtain the force histories on each wall, as well as the total vertical force on the deck, as shown in Fig. 20. The leftward and upward forces are taken as positive.

According to Figs. 19 and 20, on the front wall, the single-peak impacts of U and P-T, as well as the double-peak impacts of P-F and B are confirmed. While the wave faces with similar shapes lead to similar pressure patterns for U, P-T and P-F, P-T shows the largest magnitude and longer impact duration. The air entrapment leads to the transient high pressures on the front wall for P-F impact type (Fig. 19), resulting in large horizontal forces with magnitudes larger than those induced by the wave face (Fig. 20). The pressures and forces of B impact type are relatively lower than the other three types. It is noted that the overall high pressures among all four types are observed in P-T and P-F types, which are the results of wave face impact and air compression, respectively. Compared with the air compression and tongue tip impact, the wave face impact shows longer impact durations with large pressure and force, making it the crucial component during the whole impact process on the front wall.

On the bottom wall, the highly similar wave faces for all four types (see Fig. 9), result in the nearly identical pressure distributions and force histories (second columns of Figs. 19 and 20, respectively), as expected. As the length of the deck (a = 0.5 m), is much larger than the front wall thickness (b = 0.12 m), the pressure and force on the bottom wall show much longer impact durations (Fig. 19), and impact regions (Fig. 9), than those on the front wall. Thus, the magnitudes of the vertical forces on the deck are comparable with those on the front wall (Fig. 20), although the pressure maxima on the bottom wall are lower than that of the front wall (Fig. 19). The high-pressure areas on the bottom wall advances with the wave face without significant change of magnitude (red dot-dashed boxes, Fig. 19). The negative pressure areas appear from ~ t_0 + 0.20 s, and only cover a small area of the bottom wall without noticeable change of locations (red solid boxes in the middle column of Fig. 19), resulting in a weak downward suction force (second columns of Figs. 19 and 20).

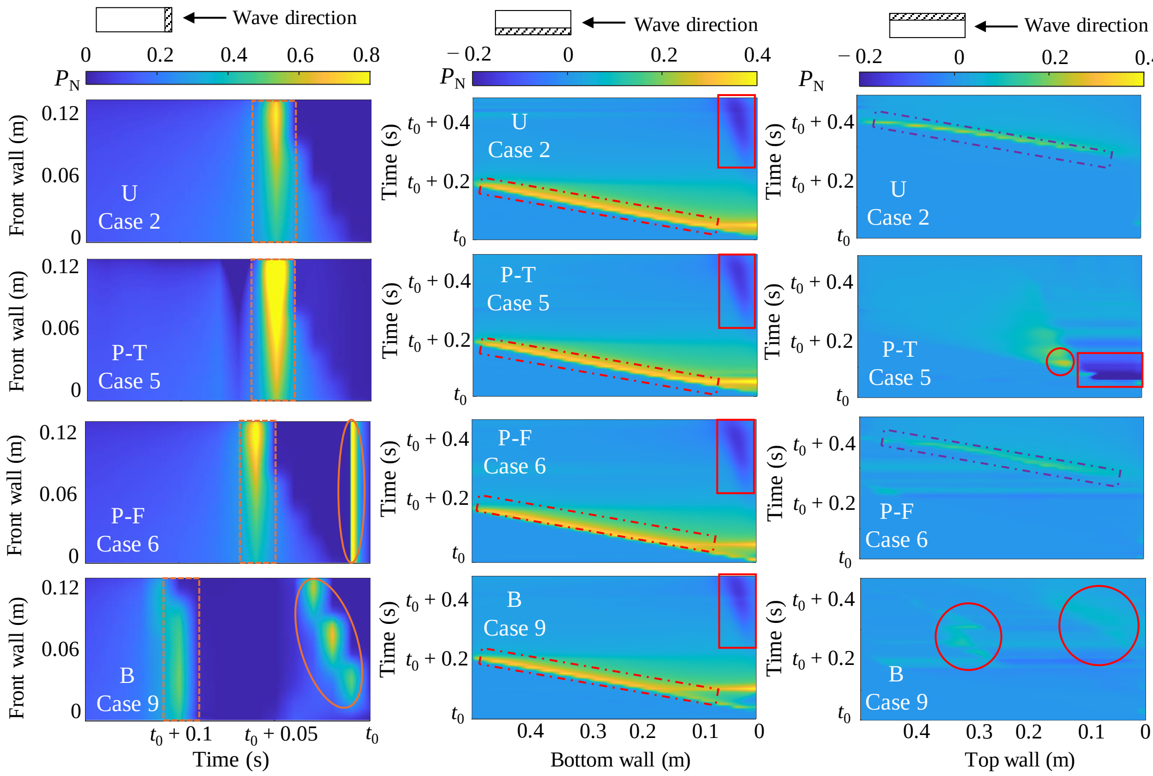

Fig. 19. Spatial and temporal pressure distributions of the representative cases of each impact type (left column: front wall; middle column: bottom wall; right column: top wall).

On the top wall, the magnitudes of pressures and forces are generally much lower than those on the front and bottom walls (Fig. 20). High similarities are found between the pressures of U and P-F types, which are featured by an advancing high-pressure area (purple dot-dashed boxes, right column of Fig. 19). This is because the wave tongues are significantly stretched vertically, and slam on the top wall instead of hitting the top wall with the tongue tip (see Fig. 9). P-T type demonstrates the most violent impact process on the top wall, as large positive and negative pressure areas appear at the same time in neighbouring locations (red solid circle and red solid box in P-T type, Fig. 19), which corresponds with tongue tip impact and air entrapment, respectively. For the B type, the pressures come from the fallen tongue tip and overtopping of the wave face (red solid circles in B type, Fig. 19), whose magnitudes are similar to the other three types. Particularly, P-T shows significant upward forces on the top wall from ~ t_0 + 0.01 s, due to the upward suction effect above the front-top corner. Combined with the upward force on the bottom wall, very large force peaks on the whole deck appear at ~ t_0 + 0.07 s (Fig. 20).

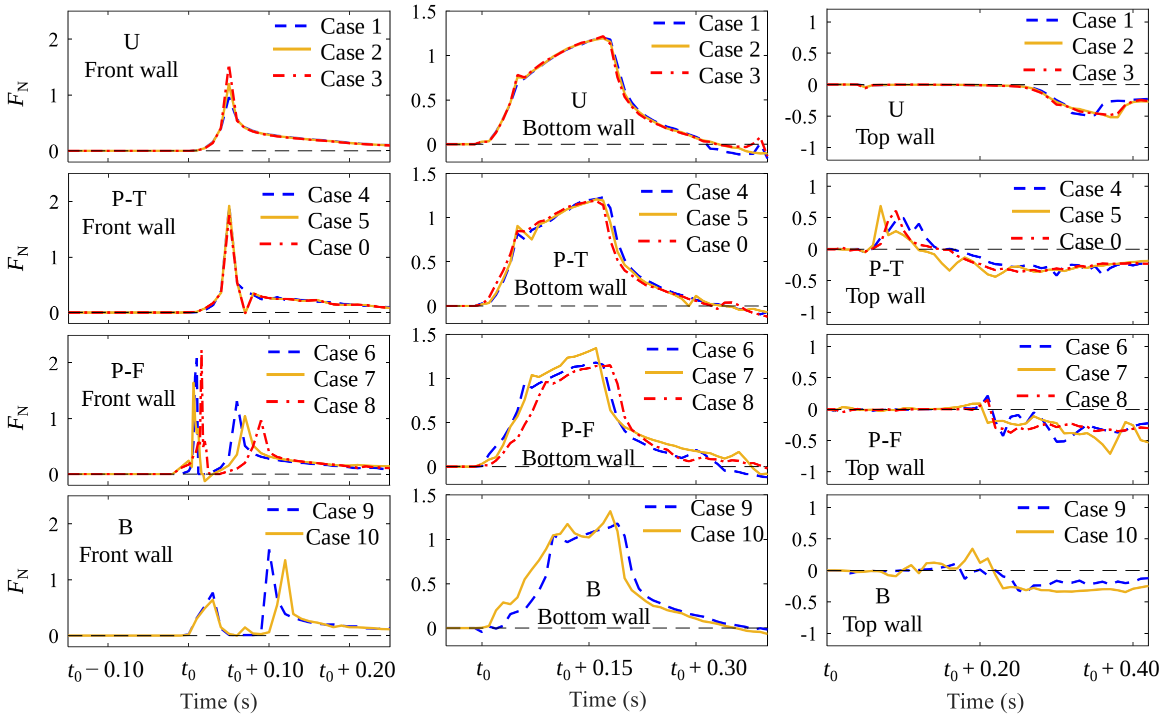

Fig. 20. Force histories on the front, bottom and top walls of all cases for the four impact types (leftward and upward forces are taken as positive).

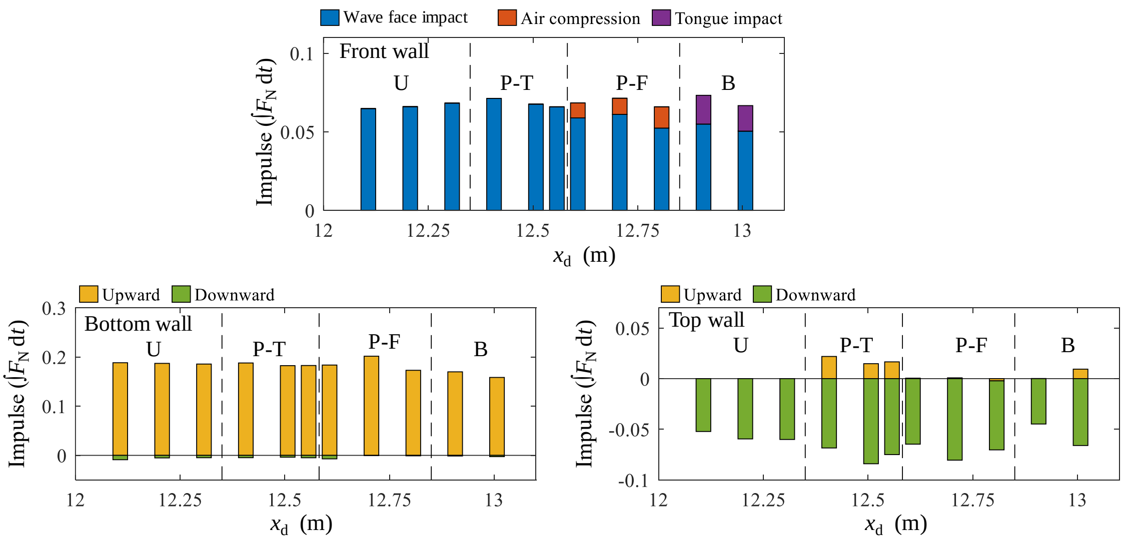

Fig. 21. Top row: Total impulses applied on front wall of the four patterns and the contributions from each elemental process; Bottom left: Total impulses applied on the bottom wall; Bottom right: Total impulses applied on the top wall.

By integrating the force histories over time, we calculate the impulse on each wall from t_0 to t_0 + 0.20 s for all cases in the four impact types. As shown in Fig. 21, we separate the impulses on the front wall by their originations (wave face, air compression or wave tongue), and the upwards and downwards impulses on the top and bottom walls are also presented separately. It can be seen that the total impulse on the front wall does not vary significantly among the four impact types (~ $0.067F_0$). It is noted that the wave face generates a lower impulse in the P-F type (due to the air cushioning effect), and the B type (the wave tongue is more developed and thus less wave energy remains in the wave face). The impulse on the bottom and top walls does not vary significantly either, while the overall mean value is $0.182F_0$ upwards on the bottom wall and $0.066F_0$ downwards on the top wall.

5.2.3. *Maximum pressures and forces*

The maximum values of pressure and force are key factors influencing structural safety, and their values on each wall for the four impact types are presented in Fig. 22. Specifically, the pressure and force on the front wall were separated by their originations.

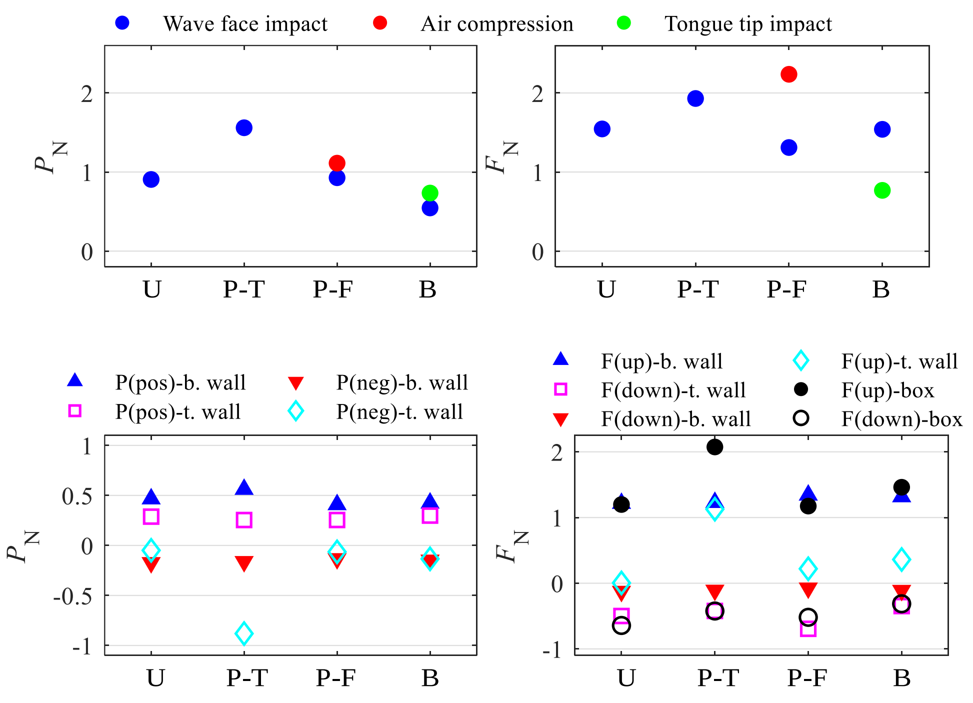

Fig. 22. First row: Maximum pressures and forces applied on the front wall in the four impact types (separated by the originations); Second row: Maximum pressures (positive and negative) and forces (upward and downward) applied on the bottom and top walls, as well as the maximum vertical forces (upward and downward) on the deck in the four impact types.

On the front wall, the impact types with well-developed plunging breakers (P-T and P-F), result in the largest pressures and forces while the other two types show lower values. The wave face impact generates pressure up to $1.560\rho c^2$ and force up to $1.932F_0$ for P-T type, and P-F shows pressure up to $1.112\rho c^2$ and force up to $2.236F_0$ due to the air compression. On the bottom wall, the maximum pressures and forces do not vary noticeably among the four impact types, due to similar impact processes. The positive and negative pressures are both significant (up to $0.561\rho c^2$ and up to $-0.172\rho c^2$, respectively), on the bottom wall, but the maximum upward force ($1.341F_0$), is much larger than the maximum downward force ($0.124F_0$). On the top wall, the positive pressure and downward force take crucial roles in all four types, with the maximum value of $0.298\rho c^2$ and $0.694F_0$, respectively. The negative pressures and upward suction forces are almost negligible for U, P-F and B types, while the P-T type shows negative pressure up to $-0.881\rho c^2$ and suction force up to $1.127F_0$, which are even comparable with those on the front and bottom walls.

6. Discussion

6.1. Characteristics of the freak wave impact on a box-shaped deck

A comparison of the impact characteristics among the impact types and structural walls is shown in Table 6. Overall, the impact on the front wall is characterised by the large transient pressure and force ($P_N > 1$ and $F_N > 1$), which spreads across the whole front wall. The impact on the bottom wall shows a longer impact duration and a wider area of contact with a slightly lower pressure ($P_N \approx 0.3$), resulting in a large upward force ($F_N > 1$). Compared with the front and bottom walls, the wave loads on the top wall are normally lower and even negligible ($P_N < 0.1$ and $F_N < 0.5$). Exceptions arise for the P-T impact type, in which the entrapped air generates large negative pressure ($P_N > 0.5$), and upward suction force ($F_N > 1$), in the vicinity of the front-top corner.

The large negative pressures and upward suction forces of P-T type impact, which have rarely been studied, amplified the tilting torque on the deck. Fig. 23 presents the pressure distributions around the wave-facing part of the deck at typical time instants. It can be seen that a large upward force on the top wall appears only ~ 0.02 s after the appearance of the maximum horizontal force, and the combination of the upward forces on the top and bottom walls results in an extreme total upward force on the deck (~ $2F_0$, see Fig. 20). It is also noted that these two upward forces are both applied on the wave-facing part of the deck, showing a relatively large distance to the deck centre. Together with the tilting torque generated by the large upward force, the P-T impact type demonstrates the largest tilting torque on the deck.

Table 6. Comparison of impact characteristics.

	Front wall	Bottom wall*	Top wall
Pressure magnitude	Large ($P_N > 1$ for all types); P-F ≈ P-T > U ≈ B	Medium ($P_N \approx 0.3$)	Low for U, P-F, B ($P_N < 0.1$); Large for P-T ($P_N > 0.5$)
Force magnitude	Large ($F_N > 1$ for all types); P-F ≈ P-T > U ≈ B	Large ($F_N > 1$)	Low for U, P-F, B ($F_N < 0.5$); Large for P-T ($F_N > 1$)
Impact duration	Very short (< 0.1 s); U ≈ P-T < P-F ≈ B	Long (~ 0.2 s)	Long (~ 0.2 s) for all types; An extra suction process for P-T (~ 0.1 s)
Origin of the wave load	Wave face impact (all types); Air compression for P-F	Wave face impact; Suction effect due to water receding	Wave tongue impact for all types; Suction effect for P-T
Large wave load location	The entire wall, especially the top part (all types)	The entire wall, especially the wave-facing part	The wave-facing part for P-T
Risk levels of impact types	P-F > P-T > U > B	P-F ≈ P-T ≈ U ≈ B	P-T >> P-F ≈ U ≈ B
Stage with high risk	The early stage of the impact (all types)	The whole impact process	The early stage of the impact for P-T

*For all impact types, the wave loads on the bottom wall show similar magnitudes and trends.

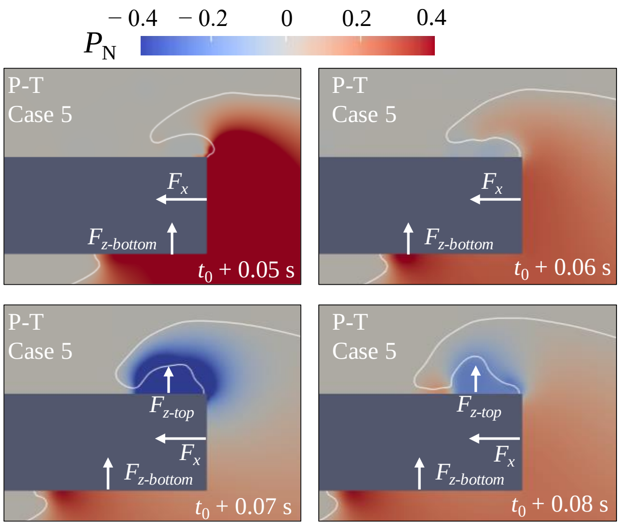

Fig. 23. Pressure distributions around the wave-facing part of the deck at the early impact stage of the P-T impact.

Overall, the amplitudes of the wave loads on the deck follow this descending order: P-T, P-F, U, B. The whole front wall and the area above the front top corner are subjected to large impact pressures, especially for P-T and P-F types. These large pressures may damage the surface walls and the devices installed there, especially for the front-top corner where the defence of the negative pressure was rarely less considered. The bottom wall experiences a large upward force with a relatively lower pressure for all four types. This large upward force leads to a large tilting torque to the deck, which may tilt the whole structure or bend the support frames. All large wave loads are likely to appear at the early stage of the impact and are mostly applied on the wave-facing side of the deck.

6.2. Influences of structure shape and incident wave profile on impact pressures

6.2.1. Influence of structure shape

Recent studies have shown that the impact behaviours depend strongly upon the shapes of the structures and waves (Martin et al., 2023; Paulsen et al., 2019; Zhang et al., 2024). Focusing on the box-shaped deck, we here discuss the roles of the vertical front wall and the sharp right angles. Taking P-T as an example, the velocity vector fields at typical time instants of Case 5 are shown in Fig. 24. It can be seen that the fluids (water and air) are forced to flow vertically along the front wall. These vertical velocities are well maintained when the fluids leave the top or bottom edge of the front wall, bringing large vertical velocities to the local fluid on the front or bottom walls. This leads to the formation of the local vortices sticking on the horizontal surfaces (top or bottom walls). According to Bernoulli's theory, these vortices result in the development of negative pressure areas, as observed in Fig. 24. The magnitude of negative pressures and their areas are highly related to the rotating velocity of the vortices.

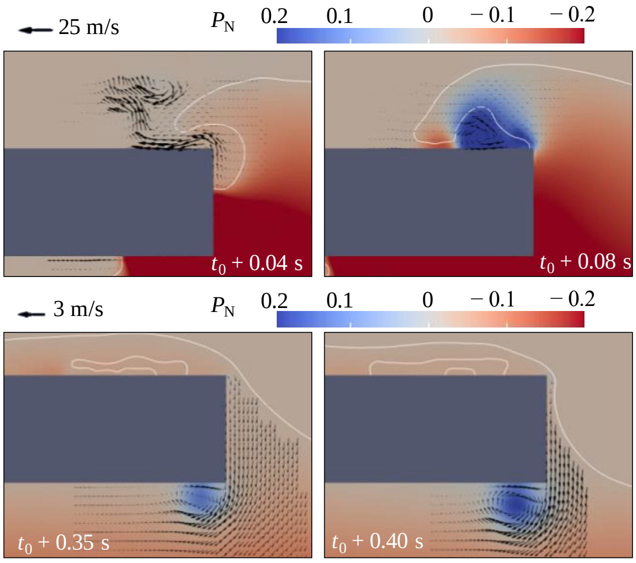

Fig. 24. Wave profiles, pressure contours and velocity vector fields at typical instants during the P-T impact (Case 5).

Compared with the wave impacts with different structure shapes, the wave impacts on vertical walls rarely report such vortices and corresponding negative pressures, as the heights of the walls are much larger, and the right angle is usually absent. Wave impacts on horizontal thin plates often show very weak negative pressure (Zhou et al., 2023; Zhou et al., 2024), as the very thin thickness of the front side is not able to develop the vertical fluid flow, thereby promoting the generation of the vortex. In contrast, in our study, the negative pressure may achieve $-0.172\rho c^2$ (on the bottom wall), even $-0.881\rho c^2$ (on the top wall). This is due to the combined influence of the front wall with a substantial thickness and the right angles on the front wall. During the impact, the thickness of the front wall (b) is large enough to develop vertical fluid flow but with a velocity that is not so large to prevent the velocity exchange between the vertical flow and the local fluid on the horizontal surfaces. The right angle on the front wall allows the vertically flowing fluid to move away from the horizontal surfaces, promoting the generation of vortices and the corresponding negative pressures. Thus, the thickness of the front wall (b), and the right angles have been identified as the key factors of the negative pressures.

The thickness of the front wall (b) has more influence on the impact behaviour. On the front wall, a small b may reduce the effectiveness of the air cushioning of the entrapped air pocket, which will be discussed in Section 6.3.1. On the bottom wall, b may influence the magnitudes of the downward suction forces. In our research, the suction forces are insignificant while the negative pressure is not negligible. However, relevant studies with similar configurations report much larger downward suction forces with a larger front wall thickness (Wang et al., 2023).

6.2.2. Influence of incident wave profile

The shape of the incident wave is another key factor dominating the impact behaviour of the wave face, entrapped air and wave tongue. The impact of the wave face induces large pressure on the front wall (especially the top part), and lower pressure on the bottom wall. It is seen that the movements of wave faces are not disturbed on the front wall for U, P-T and P-F types, as well as the bottom wall for all types. During the impact of these scenarios, the shapes of the wave faces are highly similar, leading to almost identical pressure evolutions. It is noted that the largest pressure always appears slightly behind the advancing wave face (both front and bottom walls). The impact of the overturning tongue is featured by the high pressure on a small area of contact, related to the size of the wave tongue.

A well-developed plunging breaker not only induces large pressure and force due to the intensive impact of wave face, but also leads to the air entrapment on structure walls, resulting in instantaneous pressure change and evenly distributed high pressures on the areas covered by the pocket. Thus, the incident waves with well-developed plunging breakers (e.g., the P-T and P-F types) can apply the most destructive loads to the structure.

6.3. Air entrapment behaviours at different locations

6.3.1. On the front wall: high pressure and insignificant air cushioning

The air entrapment in P-F type induces large pressures and forces on the front wall (see Section 5). To investigate the role of the entrapped air, as well as the large loads generated by the air pocket, we conduct an extra comparative study. Based on Case 6 of P-F type, we perform an extra numerical case (Case 6B), in which the b is reduced from 0.12 m to 0.115 m, giving a slightly larger δ_2. We expect such a small change to connect the entrapped air and atmosphere (hence prevent the formation of the enclosed air pocket), without noticeable influence on the impact morphology.

Fig. 25 compares the results of Case 6 and Case 6B, including the pressure and forces histories, as well as the evolutions of pressure, velocity and water-air interfaces during the development of the air pocket. It is clearly seen the two cases are identical upon the impact (t_0). However, the air between the front wall and wave face shows a larger velocity, and escapes from the top corner with a high velocity in Case 6B at t_0 + 0.01 s, and the pressure rise in the air pocket is insignificant. Comparing the pressure and force histories, it is seen that the air in Case 6B produces a much lower pressure peak (~ $0.25\rho c^2$), and force peak (~ $0.5F_0$), while the wave face impinges on the front wall with a slightly earlier time (~ 0.01 s), and induces larger pressure and force peaks.

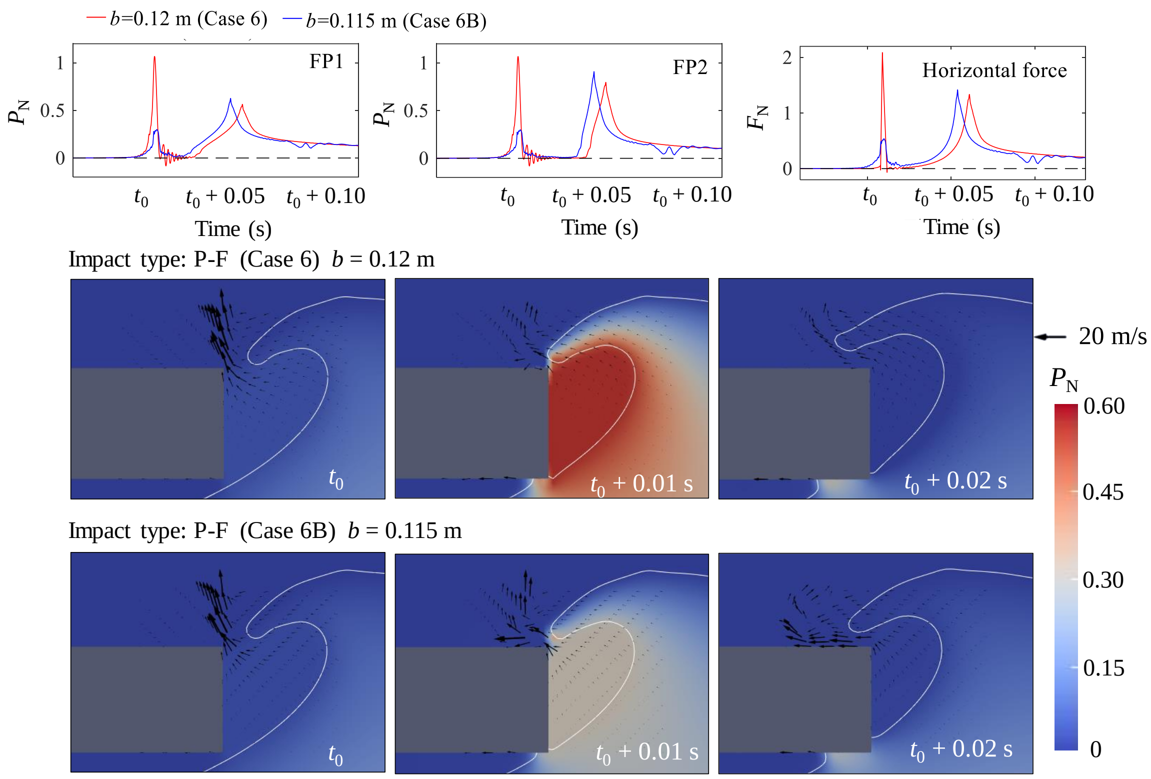

Fig. 25. Top row: pressure histories at FP1 and FP2 and horizontal force histories for the Cases 6 and 6B; Middle and bottom rows: pressure contours, velocity vectors and water-air interfaces at typical time instants for Case 6 (middle) and Case 6B (bottom).

Comparing Case 6 and Case 6B, the cushioning effect of the entrapped air pocket is confirmed, which reduces the impact pressure and force of the wave face, and delays the time of wave face impact. However, the influence of this cushioning effect is insignificant. The high pressure only appears for a short time (< 0.01 s), because the entrapped air escaped from the top edge of the front wall with a high velocity (> 10 m/s), leading to a rapid pressure drop that can be deduced from Bernoulli's theory. It is also noted that the compressed air pocket induces large pressures and forces prior to the impact of the wave face (see Figs. 25 and 10).

Current researches on aerated wave impact often report air cushioning effects (Bredmose et al., 2015; Liu et al., 2019; Ma et al., 2016). The enclosed air pockets may last for certain durations and experience continuous expansion and compression (Zhou et al., 2024), which significantly reduce wave impact pressures, resembling a mass-spring-type system (Lugni et al., 2010). However, in our study of wave impact with the air entrapment on the front wall of the deck, we only observe a very slight reduction of the pressures and forces induced by wave impact (see Fig. 25). This is because the entrapped air pocket only exists for a very short duration. The thickness of the front wall is not large enough, and the compressed air can easily re-establish the connection with the atmosphere. The entrapped air is only compressed once and is not able to expand, breaking the mechanism of the 'mass-spring-type system'.

Moreover, the air entrapment on the front wall induced very high pressure on the structure (even larger than those induced by the wave face), accompanied with very rapid pressure and force changes.

Zhou et al. (2024) also report large pressure inside the entrapped air pocket. Termed by 'air amplifying effect', the large pressure results from the superposition of the pressure oscillation and water impact pressure. Different from them, our study has shown that air entrapment can induce extreme pressure without the contribution of wave face impact, and the entrapped air pocket is much larger than those reported by Zhou et al. (2024). To sum up, during the wave impact on a box-shaped structure, the deck may not benefit from the air entrapment, instead, the air entrapment may even bring significant threat to the structure.

6.3.2. On the top wall: upward suction force

As shown in Fig. 24, the development of the large negative pressure on the top wall of the P-T type is highly related to the captured high-velocity air vortex. This negative pressure does not only apply upward suction force on the top wall but also applies downward suction force to the water tongue above. As a result, the overturning tongue collapses to the top wall very fast in the P-T type, compared with the other three impact types (see Fig. 9).

Fig. 26 presents the evolutions of pressure, velocity vectors and the water-air interface of P-T type (Case 5), demonstrating the development of the air vortex in detail. The advancing wave face leads to the air escapement from the front-top corner with a high velocity (t_0 + 0.01 s), and the movement of this air jet is restricted, and this air jet is shortly captured by the overturning tongue (t_0 + 0.03 s and t_0 + 0.05 s). The captured air is then isolated from the atmosphere by the wave tongue and structure wall, resulting in the high-velocity vortex and large negative pressure (t_0 + 0.07 s). The deceleration of the air vortex then leads to the reduction of the negative pressure (t_0 + 0.09 s and t_0 + 0.11 s).

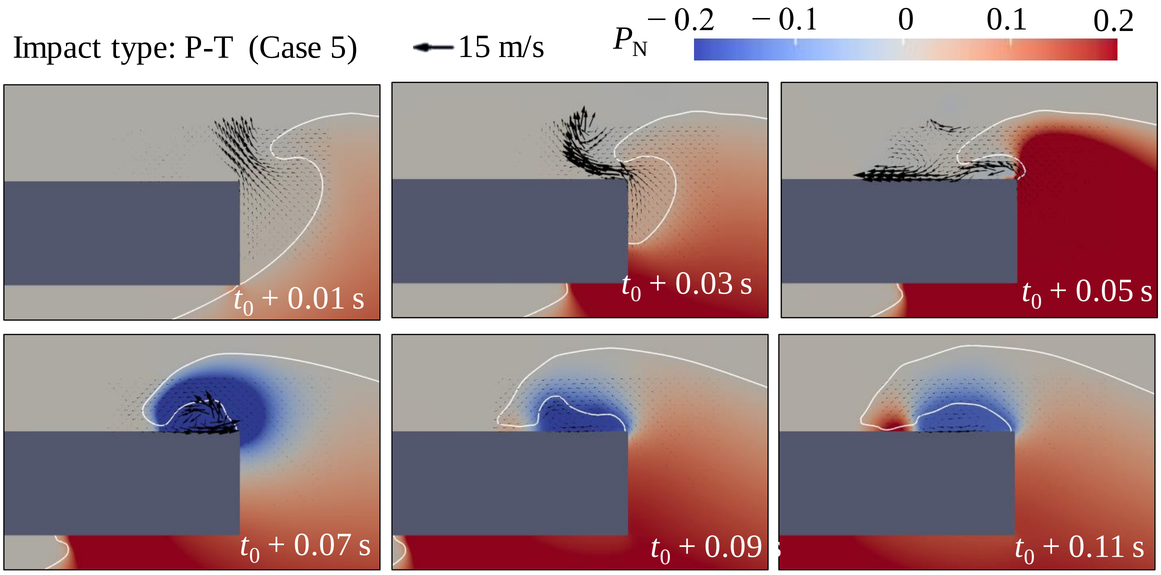

Fig. 26. Evolution of pressure contours, velocity vectors and the water-air interfaces for Case 5.

Compared with the air entrapment on the front wall, the entrapped air pocket on the top wall shows a much higher velocity (up to ~ 25 m/s) and exists for a much longer duration (> 0.1 s), than the air entrapment on the front wall (~ 0.01 s). It is also noted that the negative pressure on the top wall shows high similarity with the so-called 'suction effect' on the bottom wall (Sun et al., 2019), as they are both related to the fluid vortex in the vicinity of the structures' corners. It is supposed that such negative pressures can be reduced by mitigating the vortices.

6.3.3. Between the wave face and overturning tongue: negligible pressure rise

Air entrapment also appears in the B type. However, according to the pressure and force histories (see Section 5), the entrapped air pocket in the B impact type applies insignificant influence on the structure. Fig. 27 presents the velocity vector fields and pressure contours of the P-F and B type at typical time instants. It can be seen that a high-velocity air jet is generated near the front-top corner of the deck, as the wave tongue and wave face approach the front wall in the P-F type at t_0 (see the green circle in the top-left panel of Fig. 27). This jet is then blocked by the overturning tongue (see the green circle in the top-middle panel of Fig. 27). The air pocket on the front wall becomes completely entrained, with a significant velocity reduction of the air. The advancing wave face then leads to the compression of the air pocket, resulting in the large pressure in the air pocket (and on the front wall). The wave tongue then moves upwards, re-establishing the connectivity between the air pocket and the atmosphere (see the green circle in the top-right panel of Fig. 27). The captured air then escapes with a large velocity, leading to the instantaneous pressure reduction of the air entrapment region.

In comparison, for the B type, the entrapped air can easily move with the surrounding water before and during the impact (see the bottom row of Fig. 27). Although the air jet with a large velocity is generated above the overturning tongue, there is no noticeable velocity gradient across the interface between the tongue and entrapped air (see the green rectangles in the bottom-left and middle panels of Fig. 27). The entrained air can still follow the movement of the tongue (see the green rectangle in the bottom-right panel of Fig. 27), without significant velocity change. As a result, no significant pressure rise is observed in the air pocket. It is also noticed that the captured air pocket does not directly touch the front wall for the B type upon the impact (first and second rows, Fig. 27). By the time the front wall is exposed to the air pocket, the stretching wave tongue has already begun to establish the connectivity between the air pocket and the atmosphere, which prevents the pressure rise.

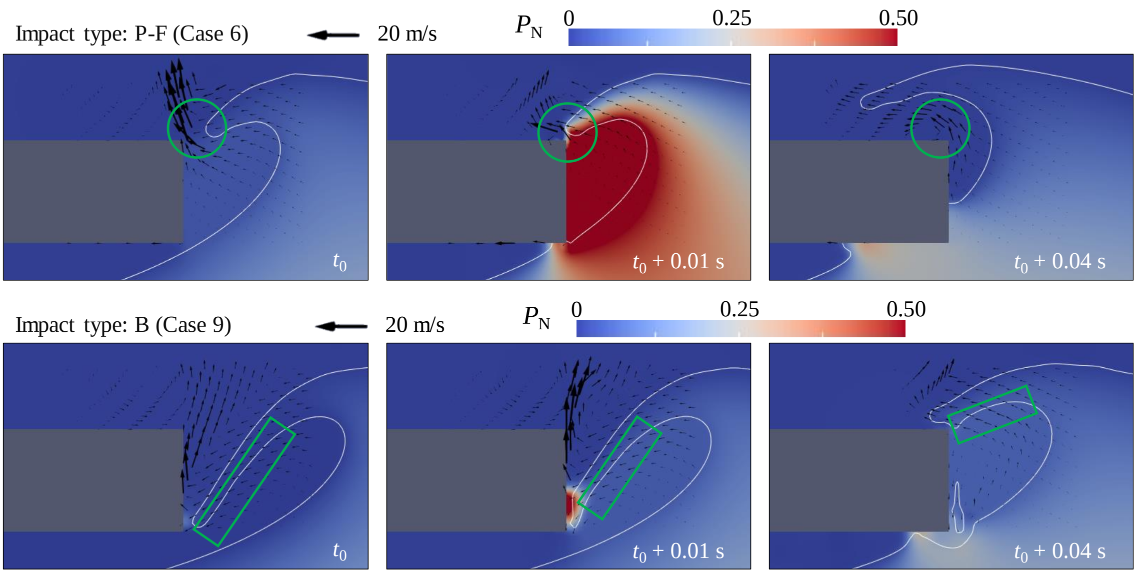

Fig. 27. Pressure and velocity contours for P-F and B type at typical time instants.

Based on the comparison between the P-F and B wave impacts, combined with the analyses of the air entrapment on the front and top walls, the following conditions are required for high pressure to develop in the air entrapment zone:

- The air pocket must be enclosed and directly connected to the structure wall;
- The movement of the inside air must be obstructed by the structure wall or the water;
- High positive pressure needs the air pocket to be compressed by the water movement and structure wall;
- High negative pressure requires the development of a high-velocity vortex in the pocket.

7. Conclusion

In this study, we develop a Finite Difference-based two-phase-flow wave flume with an enhanced momentum conservation treatment. The accuracy of the numerical wave flume was validated against the experimental data of freak wave impacts on a box-shaped deck structure, including wave profiles, wave elevations and impact pressures. By changing the horizontal location of the deck, a series of numerical simulations were performed to investigate the impact behaviours and wave kinematics and dynamics under different relative locations between the incident wave and structure.

We established a quantitative criterion for wave impact type classification. Six parameters were used to describe the morphology and movement of the wave front. Four impact types were identified, namely 'Unbroken Impact (U)', 'Plunging impact with Top wall air entrapment (P-T)', 'Plunging impact with Front wall air entrapment (P-F)' and 'Broken wave impact (B)'. U manifested the impact of unbroken waves where the wave face dominated the whole impact process and aeration did not occur; P-T and P-F stood for the wave impacts with a well-developed plunging breaker, which were featured by air entrapments on the top or front wall, respectively. B demonstrated the impact of a broken wave where the overturning tongue became evident.

The impact behaviours of these four types varied on the front and top walls but were similar on the bottom wall. The impacts on the front wall were characterised by short durations with large wave pressures and forces, while the bottom wall experienced longer impact durations, lower pressures and large forces. The vertical front wall of the deck and the sharp right angles at the deck corners promoted the generation of vortices and negative pressures on the top wall (P-T type), and bottom wall (all four types). The impacts on the top wall were insignificant if air entrapment had not happened. Overall, the descending order of the magnitudes of wave pressures and forces of the four impact types was P-T, P-F, U and B. The pressure and force magnitudes, respectively, reached up to $1.560\rho c^2$ and $2.236F_0$ on the front wall, $0.561\rho c^2$ and $1.341F_0$ on the bottom wall, $-0.881\rho c^2$ and $1.127F_0$ on the top wall (where ρ and c stand for the water density and the characteristic wave celerity, respectively; F_0 is calculated by $F_0 = 0.5\rho c^2 A$, in which A stands for the frontal projected area of the structure.). On the whole deck structure, the upward vertical force could reach $2.074F_0$.

The locations of the air entrapment significantly influenced the pressures and forces in the air entrapment region. On the front wall (P-F type), the compression of the air cavity led to large pressures. Due to the small thickness of the front wall, the air cavity only lasted for a very short duration (~ 0.01 s), leading to an insignificant cushioning effect and hence the pressures and forces due to the direct impact of wave face were slightly reduced. On the top wall (P-T type), a vortex region with relatively high flow velocities and evident negative pressures was observed in the air cavity, leading to the upward suction force. The air cavity between the overturning tongue and the wave face (B type), generated insignificant pressures. These phenomena underscore the importance of considering the air-structure interaction in assessing the impact loads generated by freak waves.

The present numerical model will be further improved to enable reliable simulation of small-scale water droplets and air bubbles such that the fluid kinematics and dynamics during breaking wave impacts can be studied in more detail. Besides, the local fluid compressibility will be considered such that numerical simulations can better reproduce the scale effects.

Acknowledgement

This research was partially supported by the National Key R&D Program of China (Grant No. 2023YFC3081300) and the National Natural Science Foundation of China (Grant No. 12302319). The first author would like to thank the Centenary Scholarship from the Faculty of Science and Engineering of Swansea University. The first author and corresponding author appreciate the technical support from the HPC Centre of Zhejiang University at Zhoushan Campus.

Supplementary data

The time series of the piston-type wavemaker motion of the experimental case (i.e., Case 0 in Section 5) measured in the experiment can be downloaded from the supplementary material.

CRediT authorship contribution statement

Xin Wang: Conceptualization, Data curation, Formal analysis, Investigation, Methodology, Software, Validation, Visualization, Writing – original draft, Writing – review & editing. **Min Luo**: Conceptualization, Data curation, Formal analysis, Funding acquisition, Investigation, Methodology, Project administration, Resources, Supervision, Validation, Writing – original draft, Writing – review & editing. **Harshinie Karunarathna**: Conceptualization, Supervision, Writing – review & editing. **Jose Horrillo-Caraballo**: Investigation, Writing – review & editing. **Dominic E. Reeve**: Conceptualization, Investigation, Methodology, Resources, Supervision, Writing – review & editing.

References

Aggarwal, A., Chella, M. A., Bihs, H., & Myrhaug, D. (2020). Properties of breaking irregular waves over slopes. Ocean Engineering, 216, 108098.

Ahmad, N., Kamath, A., & Bihs, H. (2020). 3D numerical modelling of scour around a jacket structure with dynamic free surface capturing. Ocean Engineering, 200, 107104.

Almashan, N., Neelamani, S., & Al-Houti, D. (2021). Experimental investigations on wave impact pressures under the deck and global wave forces and moments on offshore jacket platform for partial and full green water conditions. Ocean Engineering, 234, 109324.

Attili, T., Heller, V., & Triantafyllou, S. (2023a). Wave impact on rigid and flexible plates. Coastal Engineering,182, 104302.

Attili, T., Heller, V., & Triantafyllou, S. (2023b). Scaling approaches and scale effects in wave–flexible structure interaction. Journal of Fluids and Structures, 123, 103987.

Baarholm, R., & Faltinsen, O. M. (2004). Wave impact underneath horizontal decks. Journal of Marine Science and Technology, 9, 1-13.

Bagnold, R. A. (1939). Interim report on wave-pressure research. (includes plates and photographs). Journal of the Institution of Civil Engineers, 12(7), 202-226.

Bardina, J.E., Huang P.G. & Coakley T.J. (1997). Turbulence modelling validation. AIAA Paper, 97-2121.

Berthelsen, P. A., & Faltinsen, O. M. (2008). A local directional ghost cell approach for incompressible viscous flow problems with irregular boundaries. Journal of Computational Physics, 227(9), 4354-4397.

Bihs, H., Kamath, A., Chella, M. A., Aggarwal, A., & Arntsen, Ø. A. (2016). A new level set numerical wave tank with improved density interpolation for complex wave hydrodynamics. Computers & Fluids, 140, 191-208.

Bitner-Gregersen, E. M., & Gramstad, O. (2015). Rogue Waves: Impact on Ships and Offshore Structures; DNV GL Strategic Research & Innovation Position Paper 05-2015. DNV. GL, 05-2015.

Blackmore, P. A. & Hewson, P. J. (1984). Experiments on full-scale wave impact pressures, Coastal Engineering, 8(4), 331–346.

Bredmose, H., Bullock, G. N., & Hogg, A. J. (2015). Violent breaking wave impacts. Part 3. Effects of scale and aeration. Journal of Fluid Mechanics, 765, 82-113.

Bullock, G. N., & Bredmose, H. (2024). Violent breaking-wave impacts. Part 4: A detailed analysis and comparison of field and 1:4 scale measurements on sloping and vertical walls including the influence of air and scale effects. Coastal Engineering, 191, 104520.

Bullock, G. N., Obhrai, C., Peregrine, D. H., & Bredmose, H. (2007). Violent breaking wave impacts. Part 1: Results from large-scale regular wave tests on vertical and sloping walls. Coastal Engineering, 54(8), 602-617.

Chen, Y., Wu, Y., Bahuguni, A., Gullman-Strand, J., Lv, X., Lou, J., & Ren, W. (2018). Directional wave-in-deck loading on offshore structures with porous and plated decks with supporting I-beams. Coastal Engineering, 137, 79-91.

Chorin, A. J. (1968). Numerical solution of the Navier-Stokes equations. Mathematics of Computation, 22(104), 745-762.

Chuang, W. L., Chang, K. A., & Mercier, R. (2017). Impact pressure and void fraction due to plunging breaking wave impact on a 2D TLP structure. Experiments in Fluids, 58(6), 1-17.

Cui, T., He, G., Jiang, M., Wang, W., Yuan, L., Han, D., ... & Bihs, H. (2022). Large eddy simulation of focused breaking waves with different wave steepness. Ocean Modelling, 179, 102122.

Duong, T. T., Jung, K. H., Lee, G. N., Kim, H. J., Park, S. B., Shin, S., ... & Suh, S. B. (2022). Pressure estimation of wave-in-deck loading using velocity fields obtained by particle image velocimetry. Ocean Engineering, 257, 111581.

Filip, G. P., Xu, W., & Maki, K. J. (2020). A method for the prediction of extreme wave loads on a fixed platform. Applied Ocean Research, 97, 101993.

Gottlieb, S., & Shu, C. W. (1998). Total variation diminishing Runge-Kutta schemes. Mathematics of Computation, 67(221), 73-85.

Gramstad, O., Bitner-Gregersen, E., & Vanem, E. (2017). Projected changes in the occurrence of extreme and rogue waves in future climate in the North Atlantic. Proceedings of ASME 2017 36th International Conference on Ocean, Offshore and Arctic Engineering, 57656, V03AT02A012.

Ha, Y. J., Kim, K. H., Nam, B. W., & Hong, S. Y. (2020). Experimental investigation for characteristics of wave impact loads on a vertical cylinder in breaking waves. Ocean Engineering, 209, 107470.

Hopkin, M. (2004). Sea snapshots will map frequency of freak waves. Nature, 430(6999), 492-493.

Hsiao, S. C., & Lin, T. C. (2010). Tsunami-like solitary waves impinging and overtopping an impermeable seawall: Experiment and RANS modelling. Coastal Engineering, 57(1), 1-18.

Hu, Z., Tang, W., Xue, H., Zhang, X., & Wang, K. (2017). Numerical study of rogue wave overtopping with a fully-coupled fluid-structure interaction model. Ocean Engineering, 137, 48-58.

Huang, J., & Chen, G. (2022). Identification and classification of the wave impacts on the vertical wall with overhanging horizontal slab. Ocean Engineering, 262, 112313.

Jiang, G. S., & Shu, C. W. (1996). Efficient implementation of weighted ENO schemes. Journal of Computational Physics, 126(1), 202-228.

Jones, D. K., Zou, Q., & Reeve, D. E. (2013). Computational modelling of coastal flooding caused by combined surge overflow and wave overtopping on embankments. Journal of Flood Risk Management, 6(2), 70-84.

Jose, J., & Choi, S. J. (2017). Estimation of slamming coefficients on local members of offshore wind turbine foundation (jacket type) under plunging breaker. International Journal of Naval Architecture and Ocean Engineering, 9(6), 624-640.

Khedkar, K., Mamaghani, A. C., Ghysels, P., Patankar, N. A., & Bhalla, A. P. S. (2025). Preventing mass loss in the standard level set method: New insights from variational analyses. Journal of Computational Physics, 520, 113495.

Launder, B.E. & Spalding, D.B. (1974). The numerical computation of turbulent flows. Computer Methods in Applied Mechanics and Engineering, 3(2), 269-289.

Liu, M., Jiang, C., Khoo, B. C., Zhu, H., & Gao, G. (2024). A cell-based smoothed finite element model for the analysis of turbulent flow using realizable k-ε model and mixed meshes. Journal of Computational Physics, 501, 112783.

Liu, S., Gatin, I., Obhrai, C., Ong, M. C., & Jasak, H. (2019). CFD simulations of violent breaking wave impacts on a vertical wall using a two-phase compressible solver. Coastal Engineering, 154, 103564.

Lugni, C., Brocchini, M., & Faltinsen, O. M. (2010). Evolution of the air cavity during a depressurized wave impact. II. The dynamic field. Physics of Fluids, 22(5), 056102.

Luo, M., Koh, C. G., Lee, W. X., Lin, P., & Reeve, D. E. (2020). Experimental study of freak wave impacts on a tension-leg platform. Marine Structures, 74, 102821.

Luo, M., Rubinato, M., Wang, X., & Zhao, X. (2022). Experimental investigation of freak wave actions on a floating platform and effects of the air gap. Ocean Engineering, 253, 111192.

Ma, Z. H., Causon, D. M., Qian, L., Mingham, C. G., & Ferrer, P. M. (2016). Numerical investigation of air enclosed wave impacts in a depressurised tank. Ocean Engineering, 123, 15-27.

Martin, M. B., Harris, J. C., Filipot, J. F., Hulin, F., Tassin, A., & Renaud, P. (2023). Deep water focused breaking wave loads on a fixed cylinder. Coastal Engineering, 186, 104397.

Majlesi, A., Shahriar, A., Nasouri, R., Montoya, A., Du, A., Testik, F.Y., & Matamoros, A. (2024). The evaluation of explicit parameters on Eulerian-Lagrangian simulations of wave impact on coastal bridges. Coastal Engineering 191, 104540.

Menter, F. R. (1994). Two-equation eddy-viscosity turbulence models for engineering applications. AIAA Journal, 32(8), 1598-1605.

Miquel, A. M., Kamath, A., Alagan Chella, M., Archetti, R., & Bihs, H. (2018). Analysis of different methods for wave generation and absorption in a CFD-based numerical wave tank. Journal of Marine Science and Engineering, 6(2), 73.

Mitsuyasu, H. (1966). Shock Pressure of Braking Waves. 10th Conference on Coastal Engineering, ASCE, Tokyo, Japan, 268-283.

Moideen, R., Behera, M. R., Kamath, A., & Bihs, H. (2020). Numerical simulation and analysis of phase-focused breaking and non-breaking wave impact on a fixed offshore platform deck. Journal of Offshore Mechanics and Arctic Engineering, 142(5), 051901.

Mu, D., Ning, D., & Chen, L. (2024). Experimental and numerical investigations of extreme wave impacting on a suspended structure. Coastal Engineering, 193, 104592.

Osher, S., & Sethian, J. A. (1988). Fronts propagating with curvature-dependent speed: Algorithms based on Hamilton-Jacobi formulations. Journal of Computational Physics, 79(1), 12-49.

Pang, B., Ren, Y., Shen, Y., Liu, H. R., & Ding, H. (2024). A conservative sharp interface method for incompressible viscous two-phase flows with topology changes and large density ratio. Computers & Fluids, 274, 106212.

Paulsen, B. T., de Sonneville, B., van der Meulen, M., & Jacobsen, N. G. (2019). Probability of wave slamming and the magnitude of slamming loads on offshore wind turbine foundations. Coastal Engineering, 143, 76-95.

Pringle, W. J., Yoneyama, N., & Mori, N. (2016). Two-way coupled long wave-RANS model: Solitary wave transformation and breaking on a plane beach. Coastal Engineering, 114, 99-118.

Qin, H., Tang, W., Xue, H., & Hu, Z. (2017). Numerical study of nonlinear freak wave impact underneath a fixed horizontal deck in 2-D space. Applied Ocean Research, 64, 155-168.

Raessi, M., & Pitsch, H. (2012). Consistent mass and momentum transport for simulating incompressible interfacial flows with large density ratios using the level set method. Computers & Fluids, 63, 70-81.

Reeve, D. E., Soliman, A., & Lin, P. Z. (2008). Numerical study of combined overflow and wave overtopping over a smooth impermeable seawall. Coastal Engineering, 55(2), 155-166.

Seiffert, B. R., Ertekin, R. C., & Robertson, I. N. (2015). Wave loads on a coastal bridge deck and the role of entrapped air. Applied Ocean Research, 53, 91-106.

Shao, Y., Wang, W., Wan, D., & Wang, J. (2024). Numerical investigations of breaking waves and air entrainment induced by a shallowly submerged hydrofoil. Ocean Engineering, 312, 119026.

Shen, Y. M., Ng, C. O., & Zheng, Y. H. (2004). Simulation of wave propagation over a submerged bar using the VOF method with a two-equation k–ε turbulence modeling. Ocean Engineering, 31(1), 87-95.

Sun, P. N., Luo, M., Le Touzé, D., & Zhang, A. M. (2019). The suction effect during freak wave slamming on a fixed platform deck: Smoothed particle hydrodynamics simulation and experimental study. Physics of Fluids, 31(11), 117108.

Wang, H., Santo, H., Taylor, P. H., Dai, S. S., & Chan, E. S. (2023). Experimental and numerical study of wave-in-deck loads due to oblique transient wave groups. Journal of Fluids and Structures, 120, 103914.

Wang, H., Santo, H., Taylor, P. H., Dai, S. S., Day, A. H., & Chan, E. S. (2022). Wave impacts on a solid deck in transient wave groups. Journal of Fluids and Structures, 114, 103755.

Wang, X., Luo, M., Karunarathna, H., & Reeve, D. E. (2023). An enhanced momentum conservation treatment for FDM simulation of two-phase flows with large density ratio. Journal of Computational Physics,478, 111949.

Wang, Z., Wang, W., Qiu, W., & Jiang, M. (2024). Experimental study on wave-induced loads and nonlinear effects for pier-pile group foundations of sea-crossing bridges: Wave slamming and suction effect. Coastal Engineering, 192, 104567.

Wei, K., Zhou, C., & Xu, B. (2022). Spatial distribution models of horizontal and vertical wave impact pressure on the elevated box structure. Applied Ocean Research, 125, 103245.

Goda, Y., Haranaka, S., Kitahata, M. Study of Impulsive Breaking Wave Forces on Piles. Report of Port and Harbour Research Institute, 5(6) (1966), 1-30.

Yan, B., Luo, M., & Bai, W. (2019). An experimental and numerical study of plunging wave impact on a box-shape structure. Marine Structures, 66, 272-287.

Zhang, N., Xiao, L., Cheng, Z., Wei, H., & Chen, G. (2024). Classification of breaking wave impact loads on a fixed surface-piercing square column with an overhanging deck. Coastal Engineering, 193, 104570.

Zhou, T., Ma, Z., Chen, J., & Zhai, G. (2024). Multiscale air entrainment in wave-in-deck loads. Coastal Engineering, 188, 104431.

Zhou, T., Ma, Z., Zhai, G., & Chen, J. (2023). Wave-in-deck loads induced by regular wave impact: The role of compressible air entrainment. Journal of Fluids and Structures, 122, 103974.